Depletion of Sun1/2 Induces Heterochromatin Accrual in Mesenchymal Stem Cells during Adipogenesis

Matthew Goelzer[1,4], Sean Howard[1], Anamaria Zavala[1], Daniel Conway[3], Andre J van Wijnen[2], Gunes Uzer[1]

[1]Boise State University, [2]University of Vermont, [3]Virginia Commonwealth University, [4]Oral Roberts University

Word count: 4821

Key Words: LINC, Nucleoskeleton, Nuclear Envelope, Adipogenesis, Heterochromatin, Mesenchymal Stem Cells

Funding support: AG059923, P20GM109095, NSF1929188 & 2025505

Corresponding author:

Gunes Uzer PhD

Boise State University

Department of Mechanical & Biomedical Engineering

1910 University Drive, MS-2085

Boise, ID 83725-2085

Ph. (208) 426-4461

Email: gunesuzer@boisestate.edu

Abstract

Mechanical signals regulate adipogenic differentiation of mesenchymal stem cells (MSCs). Critical to the mechano-regulation of MSCs, Linker of the Nucleoskeleton and Cytoskeleton (LINC) complexes are integral to both nucleo-cytoskeletal signal transduction and structural integrity of the nucleus. The LINC complex is made of Nesprin proteins that associate with the cytoskeleton on the outer nuclear membrane (ONM) and Sun proteins that bound to nuclear lamina and chromatin at the inner nuclear membrane (INM). In addition to their role in the LINC complex function, depletion of Sun1/2 effects chromosomal tethering to the nuclear envelope, nuclear morphology, and chromatin organization. Suggesting that Sun1/2 proteins may regulate chromatin organization and adipogenic differentiation independent of the LINC complex mediated nucleo-cytoskeletal connectivity. To test this hypothesis Sun1/2 depletion was compared to expression of a dominant-negative KASH (dnKASH) domain to decouple nucleus from cytoskeleton by inhibiting Nesprin-SUN association. Sun1/2 depletion inhibited fat droplet formation and production of adipogenic proteins such as *Adipoq,* which were supported by RNA-seq showing decreased adipogensis. In contrast dnKASH responded oppositely, increasing fat droplet formation, *Adipoq* and adipogenic gene expression. At the chromatin level, Sun1/2 depletion increased H3K9me3 levels, increased H3K9me3 foci count, and enrichment on *Adipoq.* No increase of H3K9me3 levels, foci count, or increased H3K9me3 enrichment on *Adipoq* was found during dnKASH expression. We conclude that physically decoupling of the LINC complex via dnKASH accelerates adipogenesis and that depletion of Sun1/2 increases heterochromatin accrual and inhibits adipogenesis independent of the LINC complex function.

Introduction

Linker of the Cytoskeleton and Nucleoskeleton (LINC) complex is a regulator for mechanical and biochemical signal transduction to the cell nucleus[1]. The LINC complex achieves this role in-part by connecting the nucleus to cytoskeletal proteins of actin, microtubules, and intermediate filaments. The LINC complex is composed of Sun1/2 and Nesprins[2]. Nesprin proteins are found on the outer nuclear membrane (ONM) where their N-termini are bound to cytoskeletal proteins in the cytoplasm and their C-termini are located in the perinuclear space (PNS)[3,4]. Inside the PNS KASH domain located on the C-termini of Nesprins binds to C-termini of SUN domain[5]. Sun protein N-termini spans into the inner nuclear membrane (INM) where was reported to interact with both A-type and B-type Lamins[6], emerin[7], nuclear pore complexes[8] and associate with telomeric ends of DNA at the INM within the context of DNA repair[9] and Meiosis[10,11].

Mesenchymal Stem Cells (MSCs) are multipotent cells that differentiate into musculoskeletal lineages such as myoblasts, adipocytes, osteoblasts, and chondrocytes. Regulation of MSC fate is highly dependent upon their ability to sense extracellular mechanical cues and transmit this information to the chromatin. For example, disruption of the LINC complex function via expression of the dominant-negative KASH (dnKASH) where dnKASH interferes with Sun-Nesprin binding, increases histone deacetylase (HDAC) activity in human MSCs, leading to decreased expression of the osteogenesis marker Runx2 and increased expression of the adipogenesis marker Pparg[12]. Disabling LINC function via dnKASH also impairs the

mechanical-activation of focal adhesion signaling molecules FAK and Akt[13] as well as inhibiting the nuclear import of mechanoresponsive proteins β-Catenin[14] and Yap[15] that known to have proliferative[16-18] and anti-adipogenic[19-22] functions in MSCs. Function loss similar to dnKASH overexpression is also reported after depletion of Sun and Nesprin proteins. For example, stress-induced chromatin stretching was abolished upon depletion of Sun1/2 proteins[23]. Similar to dnKASH, siRNAs against Sun1/2 impairs the activation of focal adhesion proteins FAK and Akt[13] as well as inhibiting the nuclear import of β-Catenin[24]. Yap also experiences inhibition of translocation into the nucleus during siRNA mediated depletion of Nesprin1[25].

Recent findings indicate that Sun1/2 elements through their associations with LEM domain proteins, has direct links to the chromatin and ultimately regulation of the genome[26,27]. For example in flies with LINC complex mutations , BAF localization at the nuclear envelope is eliminated in which the LEM-domain protein Otefin is excluded, resulting in elevated DNA content[28] and disrupted DNA endo-replication across myofibers[29]. In the chromatin of mammalian cells, Sun1/2 proteins tether chromatin to the nuclear envelope through direct connections to Emerin[30]. Another functional role of Sun proteins were demonstrated during meiosis where *Sun1*$^{-/-}$ mouse cells have impaired homologous synapsis during oogenesis and display disrupted telomere association[31]. These findings were supported by chromatin capture studies where depletion of Sun proteins disrupts the alignment of ends of different chromosomes via altering telomere binding to the nuclear envelope[32]. Revealing a structural role of Sun proteins in the nucleus, both our group and others have reported that depletion of

Sun1/2 decreases nuclear stiffness[33,34]. In our study, Sun1/2 co-depletion was accompanied by increased heterochromatic spot area on isolated nuclei[26], suggesting that Sun mediated changes in heterochromatin organization. As MSC differentiation requires a synergy between epigenetic control and chromatin organization [35], depleting Sun proteins may affect MSC differentiation. During adipogenesis for example, inhibition of heterochromatin H3K27me3 via methyltransferase Ezh2 inhibition results in increased protein levels of Adipoq, Fabp4, and decreased osteogeneic gene expression[36]. We have recently reported that depletion of a Sun1/2 binding partner and a nuclear envelope protein, Lamin A/C, decreases MSC adipogenesis independent of mechanical stimulation[37], suggesting that structural proteins at the INM may have mechanically independent roles to control MSC function.

Therefore, Sun1/2 proteins may have overlapping structural and mechanical roles regulating chromatin organization and MSC adipogenesis. However, it is not clear whether Sun proteins may regulate MSC differentiation through their structural role, independent of LINC complex mediated mechanical information. To investigate the LINC-independent role of Sun1/2 in regulating chromatin organization and adipogenic differentiation, we compared siRNA-mediated depletion of Sun1/2 to the over expression of the dnKASH domain to block Sun-Nesprin association[38].

Results

siSun and dnKASH expression alter nuclear morphology

We first investigated the effects of Sun1/2 depletion on nuclear morphology. Shown in **Fig. 1a** MSCs treated with siRNA targeting Sun1/2 (siSun) were stained for Sun1 (green), Sun2 (red), and DNA via Hoechst staining (blue). siSun treatment reduced Sun1 and Sun2 intensity levels by 47% (n = 1478, P < 0.0001, **Fig. 1a**) and 52% (n = 1478, P < 0.0001, **Fig. 1b**), respectively, compared to siCntl treated MSCs. siSun-treated MSCs grown in growth media (GM) experienced an increase in nuclear area by 7% (P < 0.01) and perimeter by 8% (P < 0.0001) shown in **Fig. 1d** and **1e** respectively, when compared to siCntl-treated MSCs. The nuclear circularity decreased by 9% in siSun-treated cells compared to siCntl-treated cells shown in **Fig. 1f** (p<0.001).

To understand the effects of disabling LINC function on nuclear morphology of the nucleus, mCherry-tagged dnKASH was expressed via doxycycline (Dox) inducible stably infected dnKASH plasmid in MSCs. We first established the functionality of dnKASH by measuring Nesprin mislocalization from the nuclear envelope upon +Dox treatment (**Fig.S1**). dnKASH nuclei were imaged through Hoechst staining (blue) to reveal nuclear morphology changes, shown in **Fig. 2a**. In **Fig. 2b** doxycycline treatment of MSCs in growth media (GM+Dox) had a 133% increase in mCherry intensity compared to GM MSCs with no doxycycline treatment (n = 5332, P < 0.0001). GM+Dox MSCs had a decreased nuclear area by 14% (P < 0.001, **Fig.2c**) compared to control MSCs in GM. The nuclear perimeter had a slight decrease of 1% in the GM+Dox treatment group compared to the GM control group (P < 0.05, **Fig. 2d**). The circularity

also experienced a decrease of 6% in GM+Dox treatment samples compared to GM samples ($P < 0.0001$, **Fig.2e**).

Depletion of Sun1/2 Inhibits Adipogenesis

We next investigated adipogenesis in Sun1/2 depleted MSCs. Comparing the siCntl-treated MSCs cultured in growth media (siCntl GM) to MSCs cultured in adipogenic media (siCntl AM) via western blot analysis showed a robust increase of adipogenesis markers Adipoq (600%, $P < 0.01$), Cebpa (400%, $P < 0.01$), and Pparg (200%, $P < 0.01$). No increase was observed in Adipoq and Pparg in siSun-treated MSCs in adipogenic media (siSun AM) when compared to siCntl GM samples (**Fig. 3a**). Shown in **Figs 3b-c**, comparing siCntl AM and siSun AM samples showed a significant reduction of Adipoq (92%, $P < 0.01$) and Pparg (58%, $P < 0.001$) protein levels in siSun AM samples. Cebpa also experienced a decreasing but not significant trend in siSun AM samples (38%, $P = 0.22$). To further investigate the adipogic phenotype lipid droplets were imaged via lipid droplet staining (LipidSpot 488, Biotium, CA, **Fig. 3e**). Shown in **Fig. 3f**, the quantification of the mean florescent lipid droplet intensity per cell from individual imaging fields showed a 2000% increase between siCntl GM and siCntl AM treated cells ($P < 0.0001$). Lipid droplet image analysis also revealed 83% reduction of lipid droplets in the siSun AM treatment group compared to siCntl AM ($P < 0.0001$). Comparison of siSun AM and siSun GM groups showed a slight 20% increase of lipid droplet formation in siSun AM-treated MSCs ($P < 0.0001$).

dnKASH Expression Accelerates Adipogenesis in MSCs

As depletion of Sun1/2 induced decreased adipogenesis, the effects of dnKASH expression during adipogenesis was next investigated. Doxycycline alone did not alter the rate of adipogenesis differentiation in non-modified MSCs (**Fig. S2**). During adipogenesis of stably infected dnKASH-MSCs doxycycline treated samples (AM+Dox) we observed increased levels of adipogenesis markers Adipoq, Cebpa, and Pparg compared to samples grown in AM without doxycycline treatment (**Fig. 4a**). Analysis of western blots revealed significant increases of Adipoq by 98% ($P < 0.01$, **Fig. 4b**) and Pparg by 90% in the AM+Dox treated group compared to the AM controls ($P < 0.05$, **Fig. 4d**). Cepba experienced no increase in AM+Dox samples compared to AM samples ($P = 0.38$, **Fig 4c**). Comparing doxycycline-treated GM+Dox to AM+Dox samples showed increased levels of Adipoq (1000%, $P < 0.0001$), Cebpa (300%, $P < 0.01$), and Pparg (250%, $P < 0.05$). The AM group had a 500% increase in Adipoq protein levels compared to the GM treated MSCs ($P < 0.01$). Cebpa ($P = 0.28$) and Pparg ($P = 0.56$) experienced no significant increases in AM samples compared to GM samples. Shown in **Fig. 4e**, AM+Dox treatment increased fat droplets by 258% compared to AM samples ($P < 0.05$, **Fig. 4f**). Lipid droplet amounts also had significant increases in AM compared to GM (2,400%, $P < 0.0001$) and AM+Dox compared to GM+Dox (6,000%, $P < 0.0001$).

Sun1/2 Depletion Decreases Adipogenesis and Lipid Metabolism Related Genes

RNA-seq was performed on siSun and siCntl samples cultured under GM and AM conditions. DESEQ2 analyses were performed between treatment pairs and genes were filtered by having a significant gene expression differential (fold change ≥ 2-fold, P

< 0.05). Hierarchical clustering of these significant genes generated the heatmap in **Fig. 5a** which shows separated clustering of siSun and siCntl treated cells. Both siSun and siCntl sample clades display additional clustering that further separated AM and GM cultured cells, indicating different gene expression profiles under adipogenic or growth media conditions. Shown in **Fig. 5b**, variance of principle components 1 and 2 were 16.2% and 19.9%. Performing DAVID and STRING analyses to identify the most differentially expressed pathways and genes showed thirteen pathways with an FDR < 0.05 that were either significantly up regulated (**Figs. 5c & S3**) and down regulated (**Figs. 5d & S4**) in siSun AM samples compared to siCntl AM samples. As shown **Fig. 5c** and in STRING analysis (**Fig. S3**), inflammatory response was robustly upregulated in the siSun AM treatment group, potentially highlighting a regulatory role of Sun1/2 for inflammation pathways. Indicating that Sun1/2 depletion strongly inhibits adipogenic transcriptome, three out of nine down-regulated pathways in the siSun AM groups were related to adipogenesis or lipid metabolism (**Fig. 5d**, blue bars). Further highlighting a strong suppression of adipogenesis in the siSun AM group, **Fig. 5e** shows FPKM values of adipogenic or lipid metabolism genes that were both significantly expressed (fold change ≥ 1, P <0.05) and were highlighted in DAVID analysis pathway analyses (FDR < 0.05). Tables of DAVID analysis pathways can be found in **Tables S1 and S2**.

Dominant-Negative KASH Expression Upregulates Adipogenesis Related Pathways

To understand the accelerated adipogenesis during dnKASH expression, RNA-seq was performed on samples treated with or without doxycycline (±Dox) under GM and AM conditions. Like the earlier RNA-seq analysis, DESEQ2 analyses were performed

between treatment pairs and genes were filtered by having a significant gene expression differential (fold change ≥ 2-fold, $P < 0.05$). Shown in **Fig. 6a**, hierarchical heatmap of these genes showed a clustering of +Dox treatments (i.e. dnKASH expression) regardless of the media type used. AM cultured cells were further separated inside their respective ±Dox clades. Shown in **Fig. 6b**, principle component plot showed variance of principle components 1 and 2 were 25.2% and 16.9% respectively. We next performed DAVID and STRING analyses to identify the most differentially expressed pathways (FDR < 0.05). Showing an opposite that of siSun treatment, the AM +Dox treatment group had downregulated inflammatory and immune pathways, such as immune system response and response to cytokines (**Figs. 6d & S5**). Focusing on upregulated pathways showed that lipid metabolism, fatty acid metabolism and PPAR signaling were upregulated in the AM+Dox group when compared to AM only (**Figs. 6c**, blue bars). Highlighting the accelerated adipogenesis under dnKASH expression, **Fig. 6e** shows higher FPKM values of adipogenic or lipid metabolism genes that were both significantly expressed and were highlighted in both DAVID and STRING analysis (**Fig. S6**). In order to control for doxycycline effect, expression of dnKASH domain via a secondary plasmid vector that does not utilize doxycycline inducement also showed increased adipogenic marker gene expression during dnKASH expression (**Fig. S7c**). Tables of DAVID analysis pathways can be found in **Tables S3 and S4**.

H3K9me3 Levels and Enrichment at the adipogenic gene Adipoq Increases During Sun1/2 depletion

As chromatin organization is a strong regulator of differentiation, we next investigated alterations to heterochromatin and euchromatin in siSun-treated MSCs during adipogenesis. Heterochromatin markers H3K9me3, H3K27me3 and the euchromatin marker H3K4me3 were measured in Sun1/2-depleted MSCs via western blots under both GM and AM conditions (**Fig. 7a**). Comparing siCntl and siSun counterparts, siSun treatment increased H3K9me3 levels by 56% and by 86% in the AM and GM groups, respectively ($P < 0.05$, **Fig. 7b**). Shown in **Fig. 7c** siSun group also showed a 48% decrease of H3K27me3 in the AM groups ($P < 0.05$,) but no H3K27me3 changes were detected in GM groups ($P = 0.37$). No changes were detected in the euchromatin marker H3K4me3 had between siSun and siCntl treated cells under GM and AM conditions (**Fig. 7d**).

To further investigate the increased H3K9me3 levels, confocal images of H3K9me3 (green) and DNA (blue) were quantified for both siSun and siCntl groups under either GM (**Fig. 7e**) and AM conditions (**Fig. 7h**). Shown in, siSun treatment increased H3K9me3 foci count per cell by 9% ($P<0.01$, **Fig. 7f**) and foci area by 7% ($P<0.001$, **Fig. 7g**) under GM conditions. Comparing siSun and siCntl groups under AM conditions, siSun treatment increased H3K9me3 foci count per cell by 43% ($P < 0.0001$, **Fig. 7i**) while foci area remained unchanged (**Fig. 7j**). To detect any increased H3K9me3 enrichment on adipogenesis marker gene Adipoq, we next performed CUT&RUN extraction targeting H3K9me3 on siSun and siCntl treatment groups under AM conditions. Shown in **Fig. 7k**, H3K9me3 enrichment on Adipoq was increased by 156% in the siSun AM group compared to the siCntl AM group ($P < 0.05$).

H3K9me3 Levels and Enrichment at the Adipogenic Gene Adipoq Remains Unaltered During dnKASH Disruption of the LINC Complex

Investigating the increased adipogenesis of dnKASH expressing MSCs, heterochromatin markers H3K9me3, H3K27me3 and euchromatin marker H3K4me3 were measured under both GM and AM conditions (**Fig. 8a**). Contrasting to Sun1/2 depletion, western blot analysis showed a 51% decrease of H3K9me3 in the +Dox group under AM conditions ($P < 0.01$, **Fig. 8b**). Similar to siSun, AM+Dox treated dnKASH expressing MSCs decreased H3K27me3 by 56% ($P < 0.05$, **Fig. 8c**). H3K9me3 and H3K27me3 had no significant changes under GM conditions while no significant H3K4me3 differences were detected (**Fig. 8d**).

Confocal imaging of H3K9me3 (green) and DNA (Blue) during growth in GM (**Fig. 8e**) and AM (**Fig. 8h**) revealed 5% increase of H3K9me3 foci area between GM+Dox GM samples ($P < 0.05$, **Figs. 8g**) and a 7% decrease in the AM+Dox samples compared to AM samples ($P < 0.01$, **Figs. 8j**). No significant H3K9me3 foci count per cell changes were detected (**Figs. 8f &i**). Further, H3K9me3 enrichment on Adipoq was not altered between AM+Dox and AM groups (**Fig. 8k**).

Discussion

While the depletion of Sun proteins and expression of dnKASH isoforms both result in functional nucleo-cytoskeletal disconnection, independent and potentially confounding effects of the Sun1/2 proteins on differentiation and chromatin organization were

unknown. Here we show that while disabling LINC function via a dominant negative expression of KASH domain (i.e. dnKASH) biases MSC differentiation towards adipogenesis, depleting Sun1/2 proteins has an opposite effect and inhibits adipogenic differentiation as shown through western blot analysis, RNA-seq analysis, and lipid droplet counts. We further report that depletion of Sun1/2 results in increased H3K9me3 accrual at both global and gene scales. Interestingly, dnKASH treatment has no such effect. Therefore, our finding suggests that Sun proteins may direct internal nuclear functions independent of LINC complex function and these two methods cannot be used interchangeably in studying LINC function.

Previous studies have shown that depletion of Sun1/2 reduces tethering of chromosomes to the nuclear envelope[31,39,40], alters nucleolus morphology[41], and increases trimethylated K9 histone (H3K9me3) levels in hTERT-RPE1 and MCF10A cells[42]. Our results show similar trends as Sun1/2 depletion in MSCs increased both H3K9me3 protein levels and number of H3K9me3 heterochromatic foci while no H3K9me3 protein levels or foci number increases were observed under dnKASH expression. Further, we report that depleting Sun1/2 proteins at the inner nuclear envelope increases H3K9me3 heterochromatin formation on the adipogenic gene *Adipoq* in MSCs and that dnKASH expression does not alter H3K9me3 enrichment on *Adipoq*. These results reveal that Sun1/2 proteins regulates H3K9me3 heterochromatin organization independent of the LINC complex. Additionally, this observed increase of the H3K9me3, a constitutive form of heterochromatin, marks a strong response from the nucleus, indicating a potential mechanism by which adipogenesis is inhibited during

depletion of Sun1/2. As a constitutive heterochromatin form, H3K9me3 forms constitutive heterochromatin that is tightly bound to DNA[43-45], and is not easily removed. H3K27me3, on the other hand, is a facultative heterochromatin marker that is more easily modulated for differentiation[45-47]. The observed lack of H3K9me3 increase along with the corresponding decrease of H3K27me3 during dnKASH expression indicates that decoupling the LINC complex via dnKASH does not increase heterochromatin formation in MSCs. As observed in other studies, decreased heterochromatin, especially H3K27me3, is associated with increased adipogenesis. Decreases in H3K27me3 and its methyltransferase EZH2 corresponds with increased adipogenesis in MSCs[36] which EZH2 expression is directly regulated by the mechanosensitive, LINC complex regulated[24] biomolecule β-Catenin[36]. Therefore, our observed decreases of H3K27me3 during dnKASH expression with no increase in H3K9me3 may provide a mechanism by which acceleration of adipogenesis in MSCs occurs.

In our study we also found a tumorigenic and osteolytic effect from Sun1/2 depletion. During Sun1/2 depletion increases in the tumorigenic and osteolytic factors *Cxcl10*, *Cxcl1*, and *Cxcl5* were observed (Table S1). Increases in these markers are associated with increased cancer metastasis in breast cancer[48] and prostate cancer[49]. Additionally, increases of Cxcl10, Cxcl5 and Cxcl1[49] recruit cancer cell metastasis to bone[49-51], induce osteoclast differentiation[50,52] and angiogenesis[53]. Importantly, osteolysis has a direct relationship with tumorigenesis. For metastasis of cancer to occur cancer must be able to migrate out of bone or into bone[54]. Thus, osteoclasts are needed to degrade the bone matrix. Depletion of Sun1/2 leads to an upregulation of Cxcl10, Cxcl5, and Cxcl1,

However, dnKASH expression during adipogenesis saw these same genes down regulated (Table S4) indicating a reduction in the osteolytic signaling. While the underlying mechanism for these observed differences between Sun1/2 and dnKASH are unknown, these results indicate that regulation of these proto-oncogenes and the resulting osteolytic signaling is dependent upon Sun1/2 mediated connection to the internal nucleus.

This work supports previous observations[24,55,56] that inhibiting the LINC complex via siSun and dnKASH expression reduces overall nuclear structural integrity as indicated by reduced nuclear circularity or aspect ratio. Our observed increase in nuclear area and perimeter seen during Sun1/2 depletion is similar to that of our previous observations of nuclear morphology changes during Lamin A/C depletion[57]. Both Sun1/2 and Lamin A/C are important inner nuclear membrane nucleoskleton elements that associate with other structural proteins and elements such as chromatin. Previous research has shown that during both depletion of Lamin A/C and Nesprin-Sun1 association inhibition Sun1 via Sun1-KDEL expression have large deformations during micropipette direct force application, indicating a softer nuclei[34]. However, during dnKASH expression deformation of the nucleus is reduced but nucleus displacement is not recovered after removal of micropipette force[34]. Thus, showing that dnKASH expression does not significantly reduce nuclear stiffness and nuclear morphology similar to that of internuclear proteins such as Sun1/2 and Lamin A/C. Chromatin does provide structural functions in the nucleus forces during low mechanical load[58,59] and increasing heterochromatin formation has been shown to partially alter nuclear

morphology[59]. However, we have previously shown that depletion of Sun1/2 causes a reduction in nuclear stiffness and increased chromatin area size[33]. Thus, our data in combination with previous work indicates that depletion of Sun1/2 is potentially able to alter nuclear integrity independent of chromatin condensation. Additionally, our results indicate that the dnKASH expression effects on nuclear integrity is similar to other studies as seen by a reduction in nuclear area[24,55,56] , indicating dnKASH regulates nuclear morphology and function without reducing nuclear stiffness.

In conclusion, this work reveals new insight into the role of Sun1/2 proteins in the nuclear interior and its effects on the nuclear functions of differentiation and chromatin organization. Depletion of Sun1/2 not only inhibited adipogenesis, but promoted osteolytic and tumorigenic signaling. Chromatin organization was also altered, increasing H3K9me3 heterochromatin. Our findings show that these effects are independent of the LINC complex function. These results have potential impacts on our understanding of how envelopathies targeting the nuclear envelope, such as Emery-Driufus muscular dystrophy (EDMD) and Progeria, become more severe during mutations in Sun1[60]. Which, as shown here, may be cause by the misregulation of chromatin organization and differentiation regulation during Sun1/2 depletion. Thus, these results expand our understandings of the important role inner nuclear membrane proteins have in regulating proper nuclear functions and ultimately human health.

Materials and Methods

MSCs Isolation

Bone marrow derived MSCs (mdMSC) from 8-10 wk male C57BL/6 mice were isolated as described[57,61] from multiple mouse donors and MSCs pooled, providing a heterogenous MSCs cell line. Briefly, tibial and femoral marrow were collected in RPMI-1640, 9% FBS, 9% HS, 100 µg/ml pen/strep and 12µM L-glutamine. After 24 hours, non-adherent cells were removed by washing with phosphate-buffered saline and adherent cells cultured for 4 weeks. Passage 1 cells were collected after incubation with 0.25% trypsin/1 mM EDTA × 2 minutes, and re-plated in a single 175-cm2 flask. After 1-2 weeks, passage 2 cells were re-plated at 50 cells/cm2 in expansion medium (Iscove modified Dulbecco's, 9% FBS, 9% HS, antibiotics, L-glutamine). mdMSC were re-plated every 1-2 weeks for two consecutive passages up to passage 5 and tested for osteogenic and adipogenic potential, and subsequently frozen.

Stable dnKASH Cell Line

MSCs were stably transduced with a doxycycline inducible plasmid expressing an mCherry tagged dominant-negative KASH domain. dnKASH plasmid was lentiviral packaged as a generous gift from Dr. Daniel Conway. Vector map found here: https://www.addgene.org/125554/. Lentivius supernatant was added to growth media with polybrene (5 µg/ml). Lentivirus growth media mixture was added to 50-70% confluent MSCs. Lentivirus media was replaced 48 hours later with selection media containing G418 (1mg/ml) for 5 days to select stably infected dnKASH-MSCs.

393

394 *Cell Culture, Pharmacological Reagents, and Antibodies*

395 Fetal calf serum (FCS) was obtained from Atlanta Biologicals (Atlanta, GA). MSCs were
396 maintained in IMDM with FBS (10%, v/v) and penicillin/streptomycin (100µg/ml). For
397 immunostaining experiments, seeding cell density was 3,000 cells per square
398 centimeter. For adipogenic differentiation experiments, the seeding cell density was
399 10,000 cells per square centimeter. Cells were either grown in growth media (GM) or
400 adipogenic media (AM) Cells were transfected 24 hours after cell seeding with siRNA
401 targeting Sun1 and Sun2 (siSun) or a control sequence (siCntl) using RNAiMax from
402 Invitrogen. Adipogenic media was placed on siRNA treated cells twenty four hours after
403 the transfection, the adipogenic media was added which contained dexamethasone
404 (0.1µM), insulin (5 µg/ml), and indomethacin (1 µg/ml) for 5 days. For dnKASH cells,
405 cells were seeded at 10,000 cells per square centimeter. Twenty four hours after
406 seeding, dnKASH cells were given growth media containing doxycycline (1 µg/ml).
407 Adipogenic media containing dexamethasone (0.1µM), insulin (5 µg/ml), indomethacin
408 (1 µg/ml), and doxycycline (1 µg/ml) (AM+Dox) or growth media (GM+Dox) was placed
409 on dnKASH cells twenty four hours after adding initial doxycycline. Control cells were
410 grown in growth media (GM) or adipogenic media (AM) without doxycycline. Growth
411 media or adipogenic media with or without fresh doxycycline were changed every 48
412 hours.

413

414 *siRNA Silencing Sequences*

For transient silencing of MSCs, cells were transfected with gene-specific small interfering RNA (siRNA) or control siRNA (20 nM) using RNAiMax (ThermoFisher) according to manufacturer's instructions. The following Stealth Select siRNAs (Invitrogen) were used in this study: SUN1 (ThermoFischer Scientific, Assay ID #s94913), SUN2 (ThermoFischer Scientific, Assay ID s104591).

qPCR

2ul of each CUT&RUN sample was run in 20ul reaction following Bio-Rad protocols targeting Adipoq (Bio-Rad, 10025636). Briefly, 20ul reactions were made using SsoAdvanced Master Mix (Bio-Rad, 1725270). Reactions were then run at 95°C for two minutes. Then samples were heated at 95°C for 15 seconds then cooled to 60°C for 30 seconds which both steps were repeated for 40 cycles. Finally, samples were run at 60°C for two minutes. Samples were then analyzed for percent of input sample for CUT&RUN-qPCR.

RNA-seq

Five days after adipogenic treatment, following the above protocols, total RNA was extracted using RNAeasy (Qiagen) for three samples per group. Total RNA samples were sent to Novogene for mRNA sequencing and analysis. Briefly, index of the reference genome was built using Hisat2 v2.0.5 and paired-end clean 2 reads were aligned to the reference genome using Hisat2 v2.0.5. featureCounts v1.5.0-p3 was used to count the reads numbers mapped to each gene. And then FPKM of each gene was calculated based on the length of the gene and reads count mapped to this gene.

FPKM, expected number of Fragments Per Kilobase of transcript sequence per Millions base pairs sequenced. Differential expression analysis was performed using the DESeq2 R package (1.20.0). DESeq2 provides statistical routines for determining differential expression in digital gene expression data using a model based on the negative binomial distribution. The resulting P-values were adjusted using the Benjamini and Hochberg's approach for controlling the false discovery rate. Genes with an adjusted P-value < = 0.05 found by DESeq2 were assigned as differentially expressed. Genes with significant differential gene expression were further analyzed with DAVID[62] for pathway analysis. Pathways with a FDR < = 0.05 were selected.

Immunofluorescence

Twenty four hours after the siRNA treatment against Sun1/Sun2 or dnKASH expression, cells were fixed with 4% paraformaldehyde. Cells were permeabilized by incubation with 0.3% Triton X-100. Cells were incubated in a blocking serum in PBS with 5% Donkey Serum (017-000-121, Jackson Immuno Research Laboratories). Primary antibody solution was incubated on the cells for 1h at 37oC, followed by secondary antibody incubation of either Alexa Flour 594 goat anti-rabbit (Invitrogen), Alexa Fluor 488 goat anti-mouse (Invitrogen), Alexa Fluor 488 chicken anti-rabbit (Invitrogen), or Alexa fluor 594 Donkey anti-mouse (Invitrogen). For nuclear staining cells were incubated with NucBlue Hoechst stain (Fisher Scientific). Primary and secondary concentrations were both 1:300 by volume.

Image Analysis

Five days after adding adipogenic media, cells were fixed and stained with Lipid Spot 488 (Biotium, #70069), and NucBlue Hoechst stain. Images were taken using 20x objective and were exported to quantify lipid droplet formation via a custom-made MATLAB program (The MathWorks, Natick, MA), previously published[15,57] . The minimum pixel intensity of 80 was used to isolate lipid droplet staining. The mean lipid droplet intensity per cell was calculated by dividing the sum of lipid droplet stain intensity by the nuclei count per image. Exported images were used to quantify lipid droplet formation, Sun1, Sun2, mCherry, nuclear area, nuclear perimeter, and nuclear circularity via the custom-made MATLAB program previously published[57]. Cell Profiler (https://cellprofiler.org/) was used to count the number of H3K9me3 foci per cell and foci area.

Western Blotting

Whole cell lysates were prepared using radio immunoprecipitation assay (RIPA) lysis buffer (150mM NaCl, 50mM Tris HCl, 1mM EDTA, 0.24% sodium deoxycholate,1% Igepal, pH 7.5) to protect the samples from protein degradation NaF (25mM), Na3VO4 (2mM), aprotinin, leupeptin, pepstatin, and phenylmethylsulfonylfluoride (PMSF) were added to the lysis buffer. Western protein amounts were normalized to 15µg through BCA Protein Assay (Thermo Scientific, #23225). Whole cell lysates (20µg) were separated on 10% poly-acrylamide gels and transferred to polyvinylidene difluoride (PVDF) membranes. Membranes were blocked with milk (5%, w/v) diluted in Tris-buffered saline containing Tween20 (TBS-T, 0.05%). Blots were then incubated overnight at 4˚C with appropriate primary antibodies. Following primary antibody

incubation, blots were washed and incubated with horseradish peroxidase-conjugated secondary antibody diluted at 1: 5,000 (Cell Signaling) at RT for 1h in 5% milk in TBST-T. Chemiluminescence was detected with ECL plus (Amersham Biosciences, Piscataway, NJ). At least three separate experiments were used for densitometry analyses of western blots and densitometry was performed via NIH ImageJ software.

CUT&RUN

CUT&RUN was performed using the CUT&RUN Assay Kit (Cell Signaling #86652). Briefly, cells were harvested and centrifuged, washed, and bound to Concanavalin A-coated magnetic beads. Cells were then permeabilized with digitonin and incubated with primary antibody at 4°C for two hours. Cells were then washed and resuspended with pAG-MNase enzyme and incubated at 4°C for one hour. Cells were then incubated at 37°C for 10 minutes to elute DNA into solution. Solution was then extracted and purified using DNA Purification Buffers and Spin Columns (ChIP, CUT&RUN, Cell Signaling #14209). DNA samples were then used for qPCR or sequencing.

Statistical Analysis and Reproducibility

Results for densitometry were presented as mean ± SEM. Densitometry and other analyses were performed on at least three separate experiments. Differences between groups were identified by One-Way Anova. Analysis of nuclear morphology histone modifications were done using Whitney-Mann test and results were presented as mean ± STD. Differential gene expression analysis via DESEQ2 was done using Wald test. P-values of less than 0.05 were considered significant. Lipid image analysis groups were

analyzed via the Kruskal-Wallis test. CUT&RUN-qPCR was analyzed via One-Tailed Students T-Test. All experiments were conducted in triplicate to assure reproducibility.

Data Availability

RNA-Seq data that support the findings of this study have been deposited in GEO with the accession codes GSE193505.

Acknowledgements

This study was supported by AG059923, P20GM109095, NSF1929188 and, NSF 2025505

Competing interests

The author(s) declare no competing interests financial or otherwise.

Contributions

Matthew Goelzer: concept/design, data analysis/interpretation, manuscript writing

Sean Howard: data analysis, final approval of manuscript

Anamaria Zavala: data analysis/interpretation, final approval of manuscript

Daniel Conway: concept/design, final approval of manuscript

Andre J van Wijnen: concept/design, data analysis/interpretation, final approval of manuscript

Gunes Uzer: concept/design, data analysis/interpretation, financial support, manuscript writing, final approval of manuscript

Figure 1. Sun1/2 Depletion Alters Nuclear Morphology. a Representative images of MSCs treated with siRNA targeting Sun1/2 (siSun) which were stained for Sun1 (green), Sun2 (red), and DNA (blue). **b** siSun treated cells had 47% decrease of Sun1 intensity (n

= 1478, P < 0.0001). **c** Sun2 intensity levels were decreased by 52% in siSun treated cells (n = 1478, P < 0.0001). **d** MSCs treated with siSun had an increase in nuclear area by 7% (n = 1478, p 0<0.01). **e** Nucleus perimeter decreased in siSun treated MSCs by 8% (n = 1478, p<0.0001). **f** Nuclear circularity decreased by 9% in siSun treated cells (n = 1478, p<0.001). Comparisons were made against control using non-parametric Mann-Whitney Test where * P < 0.05, ** P < 0.01, *** P < 0.001, **** P < 0.0001. Scale bar represents 50μm.

Figure 2. Dominant-Negative KASH Disruption of the LINC Complex Reduces Nuclear Area. a Representative photos of doxycycline induced DNKASH cells. Images show DNKASH tagged with mCherry (Red) and DNA (Blue). **b** mCherry intensity levels increased by 133% in doxycycline treated MSCs (n = 5332, P < 0.0001). **c** Doxycycline treated MSCs experienced a 14% decrease of nuclear area (n = 5322, p 0.001). **d** Nuclear perimeter had a slight decrease of 1% in doxycycline treatment group (n = 5322, P < 0.05). **e** Nuclear circularity decreased 6% in the doxycycline treatment group (n = 5322, P < 0.0001). Comparisons were made against control using non-parametric Mann-Whitney Test where * P < 0.05, ** P < 0.01, *** P < 0.001, **** P < 0.0001. Scale bar represents 50μm.

Figure 3: Depletion of Sun1/2 Inhibits Adipogenesis. a Western analysis of adipogenesis markers Adipoq, Cebpa, and Pparg in growth media and adipogenic media during siSun and siCntl treatment. **b** Analysis of Adipoq protein levels. Comparison of adipogenic siSun and siCntl groups showed a 92% reduction of Adipoq (n = 3, P < 0.01).

555 **c** Cebpa experienced a non-significant reduction of 38% in protein levels in siSun cells
556 compared to siCntl cells during adipogensis (n = 3, p = 0.22). **d** Pparg levels decreased
557 by 58% in adipogenic siSun compared to siCntl (n = 3, P < 0.001). **e** Representative
558 images of lipid droplet florescence images where MSCs are stained for lipid droplets
559 (green) and DNA (blue). **f** Quantification of the mean florescent lipid droplet intensity per
560 cell from individual imaging fields shows a significant reduction of 83% in lipid droplet
561 amounts in adipogenic siSun treatment compared to siCntl (n = 50, P < 0.0001). Western
562 analysis group comparisons were One-Way Anova. Lipid droplet intenisty group
563 comparisons were made using Kruskal-Wallis test. * P < 0.05, ** P < 0.01, *** P < 0.001,
564 **** P < 0.0001. Scale bar represents 50μm.
565
566 **Figure 4: dnKASH Expression Induces Accelerated Adipogenesis in MSCs. a**
567 Representitive western images of doxycycline induced dnKASH cells and control cells
568 grown in growth media and adipogenic media. **b** During adipogenesis doxycycline treated
569 samples had 98% increased levels of Adipoq (n = 3, P < 0.01). **c** Pparg in doxycycline
570 treatment group during adipogenesis increased by 90% (n = 3, P < 0.05). **d** Cepba
571 experienced an increase of 27% but was not significant during adipogenesis in
572 doxycycline treatment (n = 3, p = 0.38). Representative photos of lipid droplets (green)
573 and DNA (blue). **f** Quantification of mean lipid droplet intensity per cell in each field of
574 view showed an increase of lipid droplet amounts in doxycycline treated cells by 258% (n
575 = 50, P < 0.05) during adipogensis. Western analysis group comparisons were One-Way
576 Anova. Lipid Droplet Intensity group comparisons were made using Kruskal-Wallis test. *
577 P < 0.05, ** P < 0.01, *** P < 0.001, **** P < 0.0001. Scale bar represents 50μm.

Figure 5: Sun1/2 Depletion Decreases Adipogenesis and Lipid Metabolism Related Genes. **a** Heatmap of genes with significant differential (FC > 1 and P < 0.05) gene expression during Sun1/2 depletion (n = 24). **b** Principle component plot where principal component 1 and principal component 2 explain 19.9% and 16.2% of the total variance, respectively. Prediction ellipses indicate that with a probability of 0.95, a new observation from the same group will fall inside the ellipse. *n* = 24 data points. **c** DAVID analysis of genes up regulated in siSun treatment compared to siCntl. Pathways selected have FDR < 0.05. **d** DAVID analysis of genes down regulated in siSun group compared to siCntl. Pathways selected have FDR < 0.05. Blue indicates pathways related to adipogenesis and lipid metabolism. **e** FPKM values for adipogenic and lipid metabolism related genes detected in both differential gene expression (FC > 1, P < 0.05) and in DAVID analysis (FDR < 0.05) (n = 3/grp). Group comparison was made using One-Way ANOVA where * P < 0.05.

Figure 6: Dominant-Negative KASH Expression Upregulates Adipogenesis Related Pathways. **a** Heatmap of genes with significant differential (FC > 1 and P < 0.05) gene expression during doxycycline induced dnKASH expression (n = 24). **b** Principle component plot where principal component 1 and principal component 2 explain 25.2% and 16.9% of the total variance, respectively. Prediction ellipses indicate that with a probability of 0.95, a new observation from the same group will fall inside the ellipse. *n* = 24 data points. **c** DAVID analysis of genes up regulated in doxycycline treatment compared to control. Blue indicates pathways related to adipogenesis and lipid

metabolism. Pathways selected have FDR < 0.05. **d** DAVID analysis of genes down regulated in doxycycline group compared to control. Pathways selected have FDR < 0.05. **e** FPKM values for adipogenic and lipid metabolism related genes detected in both differential gene expression (FC > 1, P < 0.05) and in DAVID analysis (FDR < 0.05) (n = 3/grp). Group comparison was made using One-Way ANOVA. * P < 0.05, ** P < 0.01.

Figure 7: Global levels of H3K9me3 and Enrichment on Adipoq increases during Sun1/2 depletion. **a** Representative western images of heterochromatin markers H3K9me3 and H3K27me3 and euchromatin marker H3K4me3 in siSun and siCntl treatments during growth in growth media and adipogenic media. **b** Western analysis of heterochromatin marker H3K9me3 revealed an increase of 56% in siSun cells compared to siCntl during adipogenesis (n = 3, P < 0.05). **c** H3K27me3 had a decrease of 48% in siSun cells compared to siCntl cells during adipogenesis (n =3, P < 0.05). **d** Euchromatin marker H3K4me3 experienced no significant changes in global protein levels between siSun and siCntl-treated cells during adipogenesis. **e** Representative images of siCntl and siSun-treated cells grown in growth media staining for H3K9me3 (green) and Hoescht (blue). **f** H3K9me3 foci count per cell in siSun cells compared to siCntl cells in growth media increased by 9% (n = 338, P < 0.01). **g** H3K9me3 foci area increased by 7% in siSun cells compared to siCntl in growth media (n = 14560, P < 0.001). **h** Representative images of siSun and siCntl-treated cells grown in adipogenic media and stained for H3K9me3 (green) and Hoechst (blue). **i** H3K9me3 foci count per cell in siSun cell compared to Sicntl Cells during adipogenesis increased by 43% (n = 213, P < 0.0001). **j**

No detectable increase of H3K9me3 foci area was found in siSun cells during adipogenesis (n = 8460). **k** CUR&RUN-qPCR targeting H3K9me3 localization on Adipoq showed an increase of 156% in siSun cells compared to siCntl (n = 3, $P < 0.05$). Western analysis group comparisons were One-Way Anova. H3K9me3 Foci count and area comparisons were made using Mann-Whitney Test. CUR&RUN-qPCR comparisons were done using One-Tailed Students T-Test. * $P < 0.05$, ** $P < 0.01$, *** $P < 0.001$, **** $P < 0.0001$. Scale bar represents 25μm.

Figure 8: H3K9me3 Levels Are Unaltered During dnKASH Disruption of the LINC Complex. a Representative images of doxycycline-induced dnKASH expression of heterochromatin markers H3K9me3 and H3K27me3 and euchromatin marker. **b** H3K9me3 levels decreased during adipogenesis in the doxycycline treatment group compared to controls by 51% (n =3, $P < 0.01$). **c** H3K27me3 levels decreased by 56% in the doxycycline treatment group compared to control during adipogenesis (n = 3, $P < 0.05$). **d** H3K4me3 levels had no significant changes in doxycycline. **e** Representative confocal imaging of H3K9me3 (green) and DNA (Blue) in growth media. **f** Analysis of H3K9me3 foci count per cell in the doxycycline treatment group in growth media showed no significant changes in foci count per cell (n= 246). **g** H3K9me3 foci area increased by 5% in the doxycycline treatment group in growth media (n = 7350, $P < 0.05$). **h** Representative images of doxycycline-treated cells and controls cells stained for H3K9me3 (green) and Hoescht (blue) during growth in adipogenic media. **i** H3K9me3 foci count per cell did not show significant changes between the doxycycline treatment group and the control group during growth in adipogenic media (n = 328). **j** The doxycycline

treatment group had decreased H3k9me3 foci area during adipogenesis by 7% compared to control (n = 11317, P < 0.01). **k** CUR&RUN-qPCR targeting H3K9me3 localization on Adipoq showed no significant increase in doxycyclinetreated cells compared to controls (n = 3). Western analysis group comparisons were One-Way Anova. H3K9me3 Foci count and area comparisons were made using Mann-Whitney Test. CUR&RUN-qPCR comparisons were done using One-Tailed Students T-Test. * P < 0.05, ** P < 0.01, *** P < 0.001, **** P < 0.0001. Scale bar represents 25μm.

References

1 Zhang, Q. *et al.* Nesprins: a novel family of spectrin-repeat-containing proteins that localize to the nuclear membrane in multiple tissues. *J Cell Sci* **114**, 4485-4498 (2001).

2 Bouzid, T. *et al.* The LINC complex, mechanotransduction, and mesenchymal stem cell function and fate. *J Biol Eng* **13**, 68, doi:10.1186/s13036-019-0197-9 (2019).

3 Mellad, J. A., Warren, D. T. & Shanahan, C. M. Nesprins LINC the nucleus and cytoskeleton. *Curr Opin Cell Biol* **23**, 47-54, doi:10.1016/j.ceb.2010.11.006 (2011).

4 Wilhelmsen, K. *et al.* Nesprin-3, a novel outer nuclear membrane protein, associates with the cytoskeletal linker protein plectin. *J Cell Biol* **171**, 799-810, doi:10.1083/jcb.200506083 (2005).

5 Cruz, V. E., Esra Demircioglu, F. & Schwartz, T. U. Structural Analysis of Different LINC Complexes Reveals Distinct Binding Modes. *Journal of molecular biology* **432**, 6028-6041, doi:10.1016/j.jmb.2020.09.019 (2020).

6 Crisp, M. *et al.* Coupling of the nucleus and cytoplasm: role of the LINC complex. *The Journal of Cell Biology* **172**, 41-53, doi:10.1083/jcb.200509124 (2006).

7 Haque, F. *et al.* SUN1 interacts with nuclear lamin A and cytoplasmic nesprins to provide a physical connection between the nuclear lamina and the cytoskeleton. *Mol Cell Biol* **26**, 3738-3751, doi:10.1128/MCB.26.10.3738-3751.2006 (2006).

8 Liu, Q. *et al.* Functional association of Sun1 with nuclear pore complexes. *J Cell Biol* **178**, 785-798, doi:10.1083/jcb.200704108 (2007).

9 Lottersberger, F., Karssemeijer, R. A., Dimitrova, N. & de Lange, T. 53BP1 and the LINC Complex Promote Microtubule-Dependent DSB Mobility and DNA Repair. *Cell* **163**, 880-893, doi:10.1016/j.cell.2015.09.057 (2015).

10 Shibuya, H. *et al.* MAJIN Links Telomeric DNA to the Nuclear Membrane by Exchanging Telomere Cap. *Cell* **163**, 1252-1266, doi:10.1016/j.cell.2015.10.030 (2015).

11 Shibuya, H., Ishiguro, K. & Watanabe, Y. The TRF1-binding protein TERB1 promotes chromosome movement and telomere rigidity in meiosis. *Nature cell biology* **16**, 145-156, doi:10.1038/ncb2896 (2014).

12 Killaars, A. R., Walker, C. J. & Anseth, K. S. Nuclear mechanosensing controls MSC osteogenic potential through HDAC epigenetic remodeling. *Proc Natl Acad Sci U S A* **117**, 21258-21266, doi:10.1073/pnas.2006765117 (2020).

13 Uzer, G. *et al.* Cell Mechanosensitivity to Extremely Low-Magnitude Signals Is Enabled by a LINCed Nucleus. *Stem Cells* **33**, 2063-2076, doi:10.1002/stem.2004 (2015).

14 Déjardin, T. *et al.* Nesprins are mechanotransducers that discriminate epithelial-mesenchymal transition programs. *J Cell Biol* **219**, doi:10.1083/jcb.201908036 (2020).

15 Thompson, M., Woods, K., Newberg, J., Oxford, J. T. & Uzer, G. Low-intensity vibration restores nuclear YAP levels and acute YAP nuclear shuttling in mesenchymal stem cells subjected to simulated microgravity. *NPJ microgravity* **6**, 35, doi:10.1038/s41526-020-00125-5 (2020).

16 Benham-Pyle, B. W., Pruitt, B. L. & Nelson, W. J. Cell adhesion. Mechanical strain induces E-cadherin-dependent Yap1 and beta-catenin activation to drive cell cycle entry. *Science (New York, N.Y.)* **348**, 1024-1027, doi:10.1126/science.aaa4559 (2015).

17 Shen, X. *et al.* YAP promotes the proliferation of neuroblastoma cells through decreasing the nuclear location of p27(Kip1) mediated by Akt. *Cell Prolif* **53**, e12734, doi:10.1111/cpr.12734 (2020).

18 Sen, B. *et al.* β-Catenin Preserves the Stem State of Murine Bone Marrow Stromal Cells Through Activation of EZH2. *Journal of bone and mineral research : the official journal of the American Society for Bone and Mineral Research*, 10.1002/jbmr.3975, doi:10.1002/jbmr.3975 (2020).

19 Lorthongpanich, C. *et al.* YAP as a key regulator of adipo-osteogenic differentiation in human MSCs. *Stem Cell Res Ther* **10**, 402, doi:10.1186/s13287-019-1494-4 (2019).

20 Pan, J. X. *et al.* YAP promotes osteogenesis and suppresses adipogenic differentiation by regulating beta-catenin signaling. *Bone research* **6**, 18, doi:10.1038/s41413-018-0018-7 (2018).

21 Sen, B. *et al.* Mechanical Loading Regulates NFATc1 and β-Catenin Signaling through a GSK3β Control Node. *Journal of Biological Chemistry* **284**, 34607-34617, doi:10.1074/jbc.M109.039453 (2009).

22 Sen, B. *et al.* Mechanical signal influence on mesenchymal stem cell fate is enhanced by incorporation of refractory periods into the loading regimen. *Journal of biomechanics* **44**, 593-599, doi:10.1016/j.jbiomech.2010.11.022 (2011).

23 Tajik, A. *et al.* Transcription upregulation via force-induced direct stretching of chromatin. *Nat Mater* **15**, 1287-1296, doi:10.1038/nmat4729 (2016).

24 Uzer, G. *et al.* Sun-mediated mechanical LINC between nucleus and cytoskeleton regulates betacatenin nuclear access. *Journal of biomechanics* **74**, 32-40, doi:10.1016/j.jbiomech.2018.04.013 (2018).

25 Driscoll, T. P., Cosgrove, B. D., Heo, S. J., Shurden, Z. E. & Mauck, R. L. Cytoskeletal to Nuclear Strain Transfer Regulates YAP Signaling in Mesenchymal Stem Cells. *Biophys J* **108**, 2783-2793, doi:10.1016/j.bpj.2015.05.010 (2015).

26 Lee, K. K. *et al.* Distinct functional domains in emerin bind lamin A and DNA-bridging protein BAF. *J Cell Sci* **114**, 4567-4573 (2001).

27 Caputo, S. *et al.* The carboxyl-terminal nucleoplasmic region of MAN1 exhibits a DNA binding winged helix domain. *J Biol Chem* **281**, 18208-18215, doi:10.1074/jbc.M601980200 (2006).

28 Unnikannan, C. P., Reuveny, A., Grunberg, D. & Volk, T. Recruitment of BAF to the nuclear envelope couples the LINC complex to endoreplication. *Development (Cambridge, England)* **147**, doi:10.1242/dev.191304 (2020).

29 Wang, S. *et al.* Mechanotransduction via the LINC complex regulates DNA replication in myonuclei. *J Cell Biol* **217**, 2005-2018, doi:10.1083/jcb.201708137 (2018).

30 Salpingidou, G., Smertenko, A., Hausmanowa-Petrucewicz, I., Hussey, P. J. & Hutchison, C. J. A novel role for the nuclear membrane protein emerin in association of the centrosome to the outer nuclear membrane. *J Cell Biol* **178**, 897-904, doi:10.1083/jcb.200702026 (2007).

31 Ding, X. *et al.* SUN1 is required for telomere attachment to nuclear envelope and gametogenesis in mice. *Dev Cell* **12**, 863-872, doi:10.1016/j.devcel.2007.03.018 (2007).

32 Zuo, W. *et al.* Stage-resolved Hi-C analyses reveal meiotic chromosome organizational features influencing homolog alignment. *Nature communications* **12**, 5827, doi:10.1038/s41467-021-26033-0 (2021).

33 Newberg, J. *et al.* Isolated nuclei stiffen in response to low intensity vibration. *J Biomech* **111**, 110012, doi:10.1016/j.jbiomech.2020.110012 (2020).

34 Neelam, S. *et al.* Direct force probe reveals the mechanics of nuclear homeostasis in the mammalian cell. *Proceedings of the National Academy of*

Sciences of the United States of America **112**, 5720-5725, doi:10.1073/pnas.1502111112 (2015).

35 Rubin, J., Styner, M. & Uzer, G. Physical Signals May Affect Mesenchymal Stem Cell Differentiation via Epigenetic Controls. *Exercise and sport sciences reviews* **46**, 42-47, doi:10.1249/jes.0000000000000129 (2018).

36 Sen, B. *et al.* β-Catenin Preserves the Stem State of Murine Bone Marrow Stromal Cells Through Activation of EZH2. *J Bone Miner Res* **35**, 1149-1162, doi:10.1002/jbmr.3975 (2020).

37 Goelzer, M. *et al.* Lamin A/C Is Dispensable to Mechanical Repression of Adipogenesis. *International Journal of Molecular Sciences* **22**, 6580 (2021).

38 Lombardi, M. L. *et al.* The interaction between nesprins and sun proteins at the nuclear envelope is critical for force transmission between the nucleus and cytoskeleton. *J Biol Chem* **286**, 26743-26753, doi:10.1074/jbc.M111.233700 (2011).

39 Cain, N. E. *et al.* Conserved SUN-KASH Interfaces Mediate LINC Complex-Dependent Nuclear Movement and Positioning. *Current biology : CB* **28**, 3086-3097.e3084, doi:10.1016/j.cub.2018.08.001 (2018).

40 Meinke, P. *et al.* Muscular dystrophy-associated SUN1 and SUN2 variants disrupt nuclear-cytoskeletal connections and myonuclear organization. *PLoS Genet* **10**, e1004605, doi:10.1371/journal.pgen.1004605 (2014).

41 Matsumoto, A. *et al.* Loss of the integral nuclear envelope protein SUN1 induces alteration of nucleoli. *Nucleus (Austin, Tex.)* **7**, 68-83, doi:10.1080/19491034.2016.1149664 (2016).

42 Satomi, E., Ueda, M., Katahira, J. & Hieda, M. The SUN1 splicing variants SUN1_888 and SUN1_916 differentially regulate nucleolar structure. *Genes to cells : devoted to molecular & cellular mechanisms* **25**, 730-740, doi:10.1111/gtc.12807 (2020).

43 Nakayama, J., Rice, J. C., Strahl, B. D., Allis, C. D. & Grewal, S. I. Role of histone H3 lysine 9 methylation in epigenetic control of heterochromatin assembly. *Science* **292**, 110-113, doi:10.1126/science.1060118 (2001).

44 Martens, J. H. *et al.* The profile of repeat-associated histone lysine methylation states in the mouse epigenome. *EMBO J* **24**, 800-812, doi:10.1038/sj.emboj.7600545 (2005).

45 Becker, J. S., Nicetto, D. & Zaret, K. S. H3K9me3-Dependent Heterochromatin: Barrier to Cell Fate Changes. *Trends Genet* **32**, 29-41, doi:10.1016/j.tig.2015.11.001 (2016).

46 Cheng, L. *et al.* Chromatin Assembly Factor 1 (CAF-1) facilitates the establishment of facultative heterochromatin during pluripotency exit. *Nucleic Acids Res* **47**, 11114-11131, doi:10.1093/nar/gkz858 (2019).

47 Yi, S. A., Han, J. & Han, J. W. Epigenetic role of nuclear S6K1 in early adipogenesis. *BMB Rep* **49**, 401-402, doi:10.5483/bmbrep.2016.49.8.116 (2016).

48 Wu, X., Sun, A., Yu, W., Hong, C. & Liu, Z. CXCL10 mediates breast cancer tamoxifen resistance and promotes estrogen-dependent and independent proliferation. *Molecular and cellular endocrinology* **512**, 110866, doi:10.1016/j.mce.2020.110866 (2020).

802 49 Hardaway, A. L., Herroon, M. K., Rajagurubandara, E. & Podgorski, I. Marrow
803 adipocyte-derived CXCL1 and CXCL2 contribute to osteolysis in metastatic
804 prostate cancer. *Clinical & experimental metastasis* **32**, 353-368,
805 doi:10.1007/s10585-015-9714-5 (2015).
806 50 Lee, J. H. *et al.* CXCL10 promotes osteolytic bone metastasis by enhancing
807 cancer outgrowth and osteoclastogenesis. *Cancer research* **72**, 3175-3186,
808 doi:10.1158/0008-5472.can-12-0481 (2012).
809 51 Romero-Moreno, R. *et al.* The CXCL5/CXCR2 axis is sufficient to promote breast
810 cancer colonization during bone metastasis. *Nat Commun* **10**, 4404,
811 doi:10.1038/s41467-019-12108-6 (2019).
812 52 Onan, D. *et al.* The chemokine Cxcl1 is a novel target gene of parathyroid
813 hormone (PTH)/PTH-related protein in committed osteoblasts. *Endocrinology*
814 **150**, 2244-2253, doi:10.1210/en.2008-1597 (2009).
815 53 Chen, C. *et al.* CXCL5 induces tumor angiogenesis via enhancing the expression
816 of FOXD1 mediated by the AKT/NF-κB pathway in colorectal cancer. *Cell death*
817 *& disease* **10**, 178, doi:10.1038/s41419-019-1431-6 (2019).
818 54 Goltzman, D. Osteolysis and cancer. *The Journal of clinical investigation* **107**,
819 1219-1220, doi:10.1172/jci13073 (2001).
820 55 Luke, Y. *et al.* Nesprin-2 Giant (NUANCE) maintains nuclear envelope
821 architecture and composition in skin. *J Cell Sci* **121**, 1887-1898,
822 doi:10.1242/jcs.019075 (2008).

56 Alam, S. G. *et al.* The mammalian LINC complex regulates genome transcriptional responses to substrate rigidity. *Sci Rep* **6**, 38063, doi:10.1038/srep38063 (2016).

57 Goelzer, M. *et al.* Lamin A/C Is Dispensable to Mechanical Repression of Adipogenesis. *Int J Mol Sci* **22**, doi:10.3390/ijms22126580 (2021).

58 Stephens, A. D., Banigan, E. J., Adam, S. A., Goldman, R. D. & Marko, J. F. Chromatin and lamin A determine two different mechanical response regimes of the cell nucleus. *Molecular biology of the cell* **28**, 1984-1996, doi:10.1091/mbc.E16-09-0653 (2017).

59 Stephens, A. D. *et al.* Chromatin histone modifications and rigidity affect nuclear morphology independent of lamins. *Molecular biology of the cell* **29**, 220-233, doi:10.1091/mbc.E17-06-0410 (2018).

60 Janin, A., Bauer, D., Ratti, F., Millat, G. & Mejat, A. Nuclear envelopathies: a complex LINC between nuclear envelope and pathology. *Orphanet journal of rare diseases* **12**, 147, doi:10.1186/s13023-017-0698-x (2017).

61 Peister, A. *et al.* Adult stem cells from bone marrow (MSCs) isolated from different strains of inbred mice vary in surface epitopes, rates of proliferation, and differentiation potential. *Blood* **103**, 1662-1668, doi:10.1182/blood-2003-09-3070 (2004).

62 Dennis, G., Jr. *et al.* DAVID: Database for Annotation, Visualization, and Integrated Discovery. *Genome Biol* **4**, P3 (2003).

Depletion of Sun1/2 Induces Heterochromatin Accrual in MSCs during Adipogenesis

Matthew Goelzer[1,4], Sean Howard[1], Anamaria Zavala[1], Daniel Conway[3] , Andre J van Wijnen[2], Gunes Uzer[1] †

[1]Boise State University, [2]University of Vermont, [3]Virginia Commonwealth University, [4]Oral Roberts University

† **Corresponding Author**

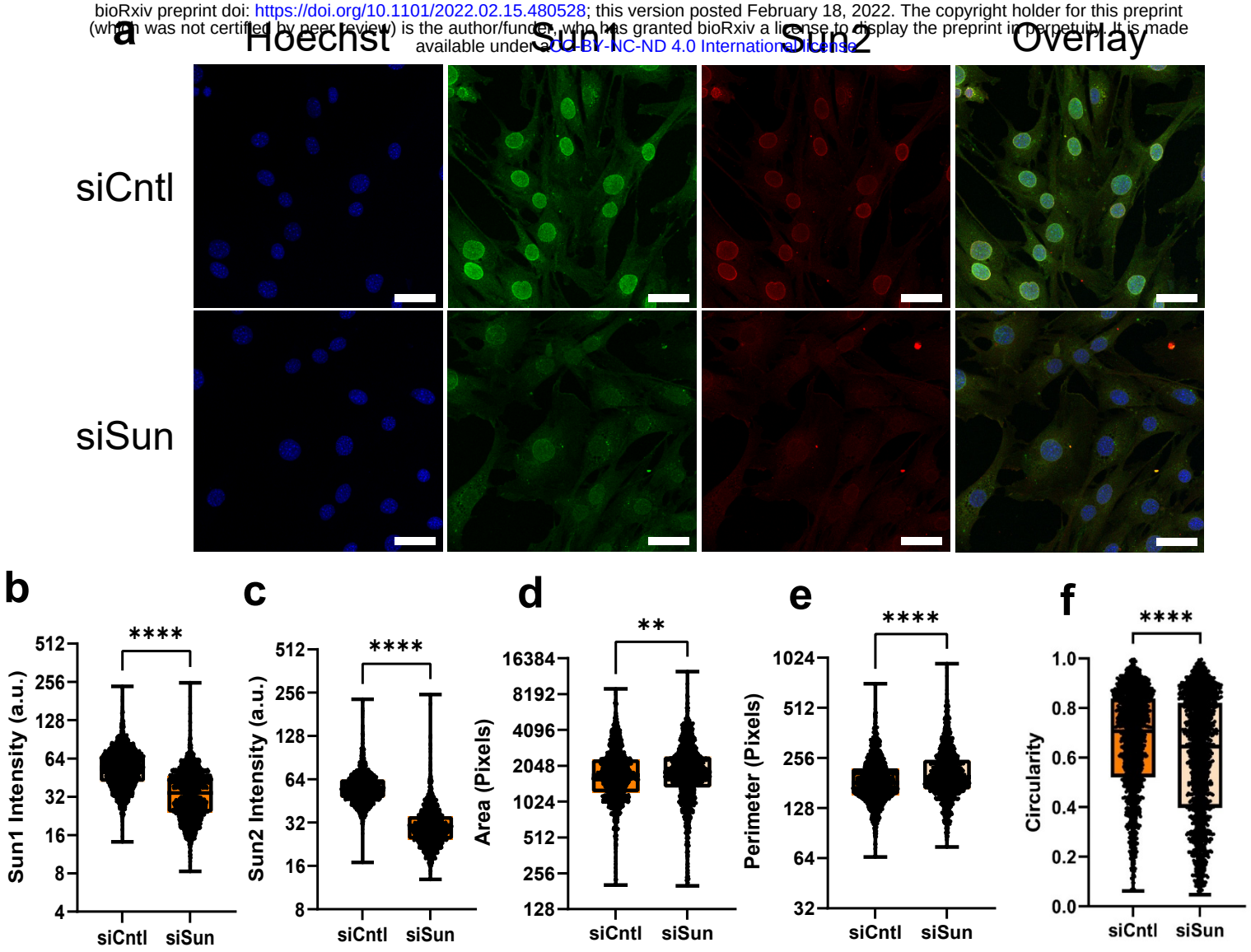

Figure 1. Sun1/2 Depletion Alters Nuclear Morphology. a Representative images of MSCs treated with siRNA targeting Sun1/2 (siSun) which were stained for Sun1 (green), Sun2 (red), and DNA (blue). **b** siSun treated cells had 47% decrease of Sun1 intensity (n = 1478, P < 0.0001). **c** Sun2 intensity levels were decreased by 52% in siSun treated cells (n = 1478, P < 0.0001). **d** MSCs treated with siSun had an increase in nuclear area by 7% (n = 1478, p 0<0.01). **e** Nucleus perimeter decreased in siSun treated MSCs by 8% (n = 1478, p<0.0001). **f** Nuclear circularity decreased by 9% in siSun treated cells (n = 1478, p<0.001). Comparisons were made against control using non-parametric Mann-Whitney Test where * P < 0.05, ** P < 0.01, *** P < 0.001, **** P < 0.0001. Scale bar represents 50μm.

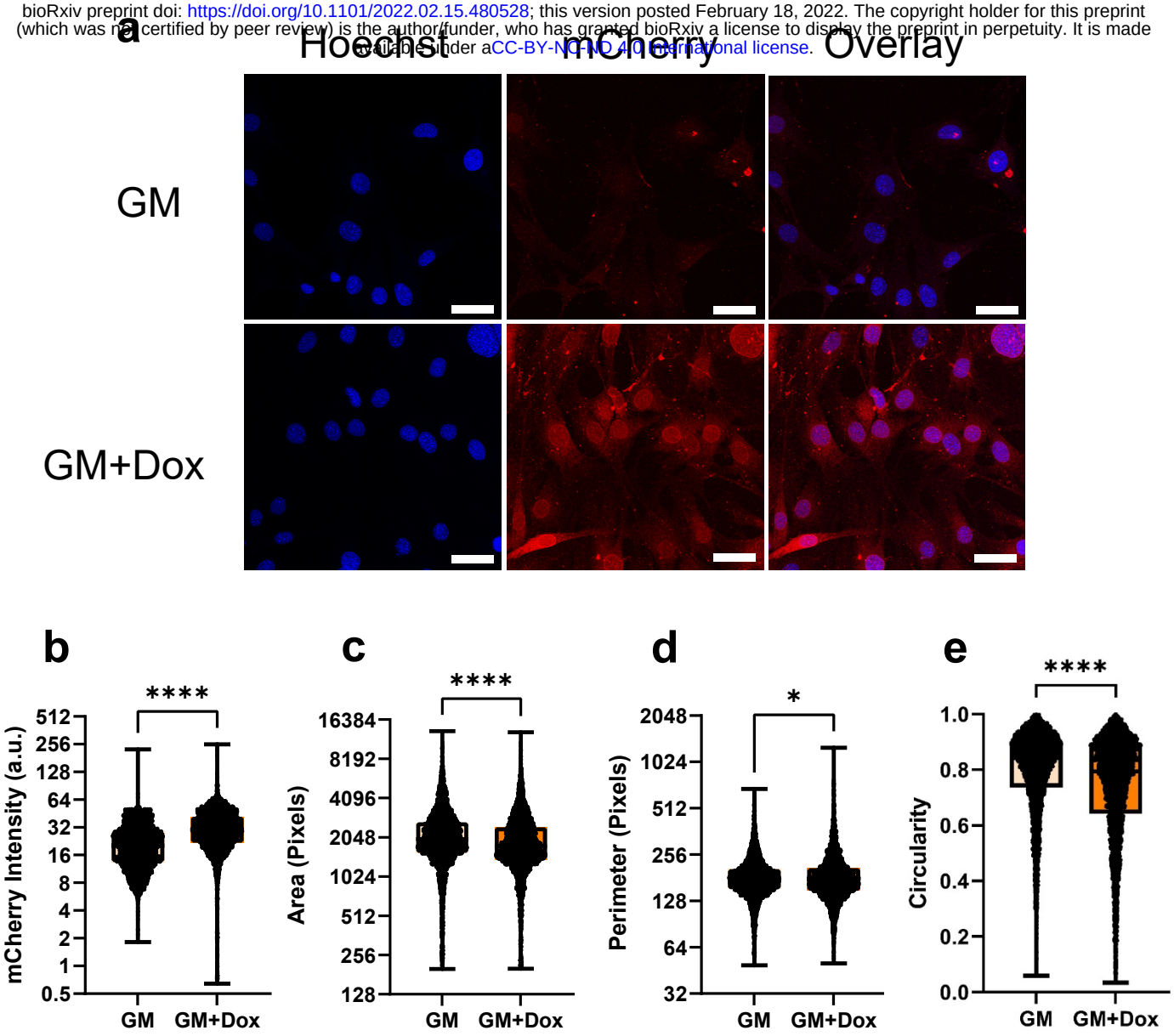

Figure 2. Dominant-Negative KASH Disruption of the LINC Complex Reduces Nuclear Area. a Representative photos of doxycycline induced dnKASH cells. Images show dnKASH tagged with mCherry (Red) and DNA (Blue). **b** mCherry intensity levels increased by 133% in doxycycline treated MSCs (n = 5332, P < 0.0001). **c** Doxycycline treated MSCs experienced a 14% decrease of nuclear area (n = 5322, p 0.001). **d** Nuclear perimeter had a slight decrease of 1% in doxycycline treatment group (n = 5322, P < 0.05). **e** The circularity experienced a decrease of 6% in doxycycline treatment group (n = 5322, P < 0.0001). Comparisons were made against control using non-parametric Mann-Whitney Test where * P < 0.05, ** P < 0.01, *** P < 0.001, **** P < 0.0001. Scale bar represents 50μm.

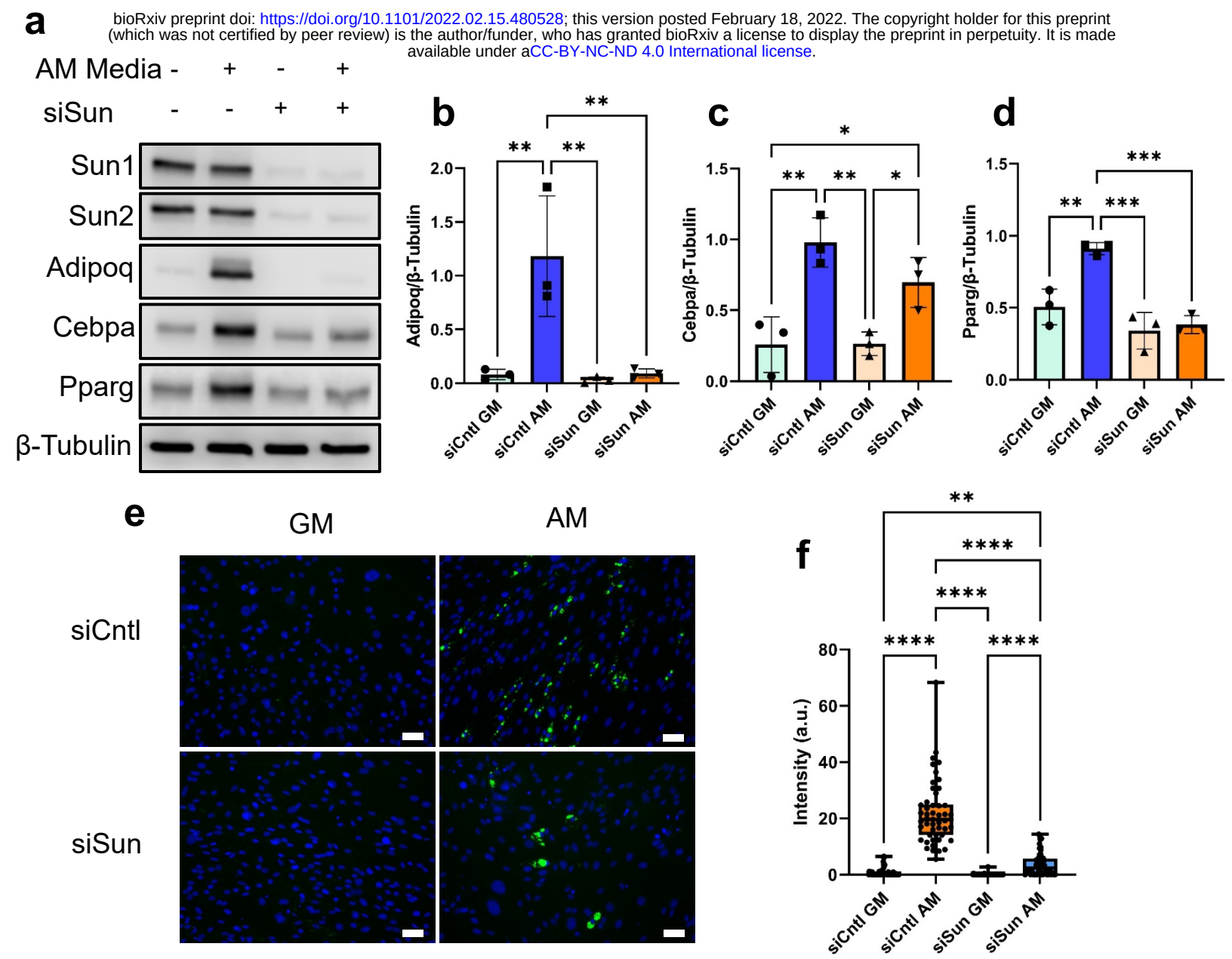

Figure 3: Depletion of Sun1/2 Inhibits Adipogenesis. a Western analysis of adipogenesis markers Adipoq, Cebpa, and Pparg in growth media and adipogenic media during siSun and siCntl treatment. **b** Analysis of Adipoq protein levels. Comparison of adipogenic siSun and siCntl groups showed a 92% reduction of Adipoq (n = 3, P < 0.01). **c** Cebpa experienced a non-significant reduction of 38% in protein levels in siSun cells compared to siCntl cells during adipogensis (n = 3, p = 0.22). **d** Pparg levels decreased by 58% in adipogenic siSun compared to siCntl (n = 3, P < 0.001). **e** Representative images of lipid droplet florescence images where MSCs are stained for lipid droplets (green) and DNA (blue). **f** Quantification of the mean florescent lipid droplet intensity per cell from individual imaging fields shows a significant reduction of 83% in lipid droplet amounts in adipogenic siSun treatment compared to siCntl (n = 50, P < 0.0001). Western analysis group comparisons were One-Way Anova. Lipid droplet intenisty group comparisons were made using Kruskal-Wallis test. * P < 0.05, ** P < 0.01, *** P < 0.001, **** P < 0.0001. Scale bar represents 50μm.

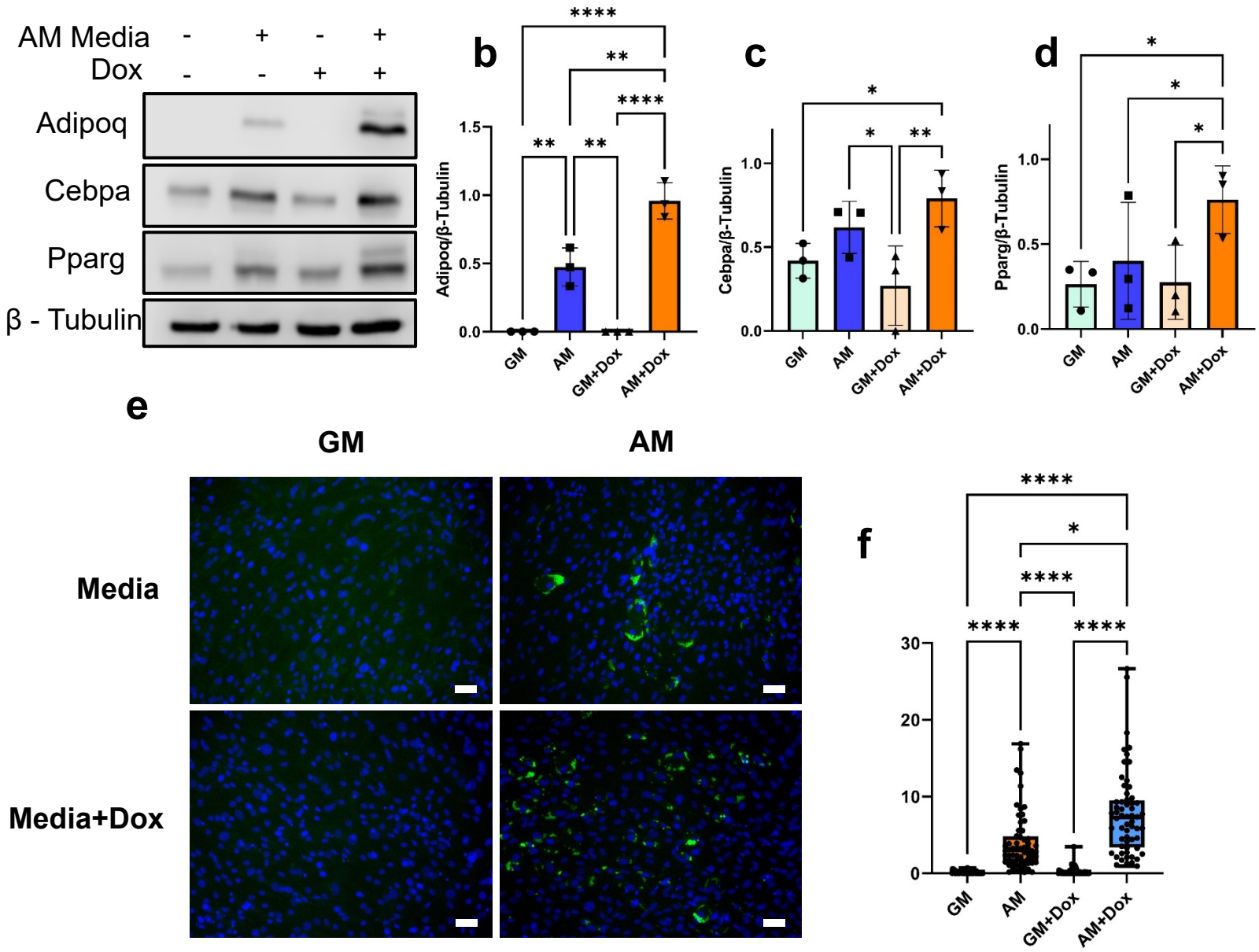

Figure 4: dnKASH Expression Induces Accelerated Adipogenesis in MSCs. **a** Representitive western images of doxycycline induced dnKASH cells and control cells grown in growth media and adipogenic media. **b** During adipogenesis doxycycline treated samples had 98% increased levels of Adipoq (n = 3, P < 0.01). **c** Pparg in doxycycline treatment group during adipogenesis increased by 90% (n = 3, P < 0.05). **d** Cepba experienced an increase of 27% but was not significant during adipogenesis in doxycycline treatment (n = 3, p = 0.38). Representative photos of lipid droplets (green) and DNA (blue). **f** Quantification of mean lipid droplet intensity per cell in each field of view showed an increase of lipid droplet amounts in doxycycline treated cells by 258% (n = 50, P < 0.05) during adipogensis. Western analysis group comparisons were One-Way Anova. Lipid Droplet Intensity group comparisons were made using Kruskal-Wallis test. * P < 0.05, ** P < 0.01, *** P < 0.001, **** P < 0.0001. Scale bar represents 50μm.

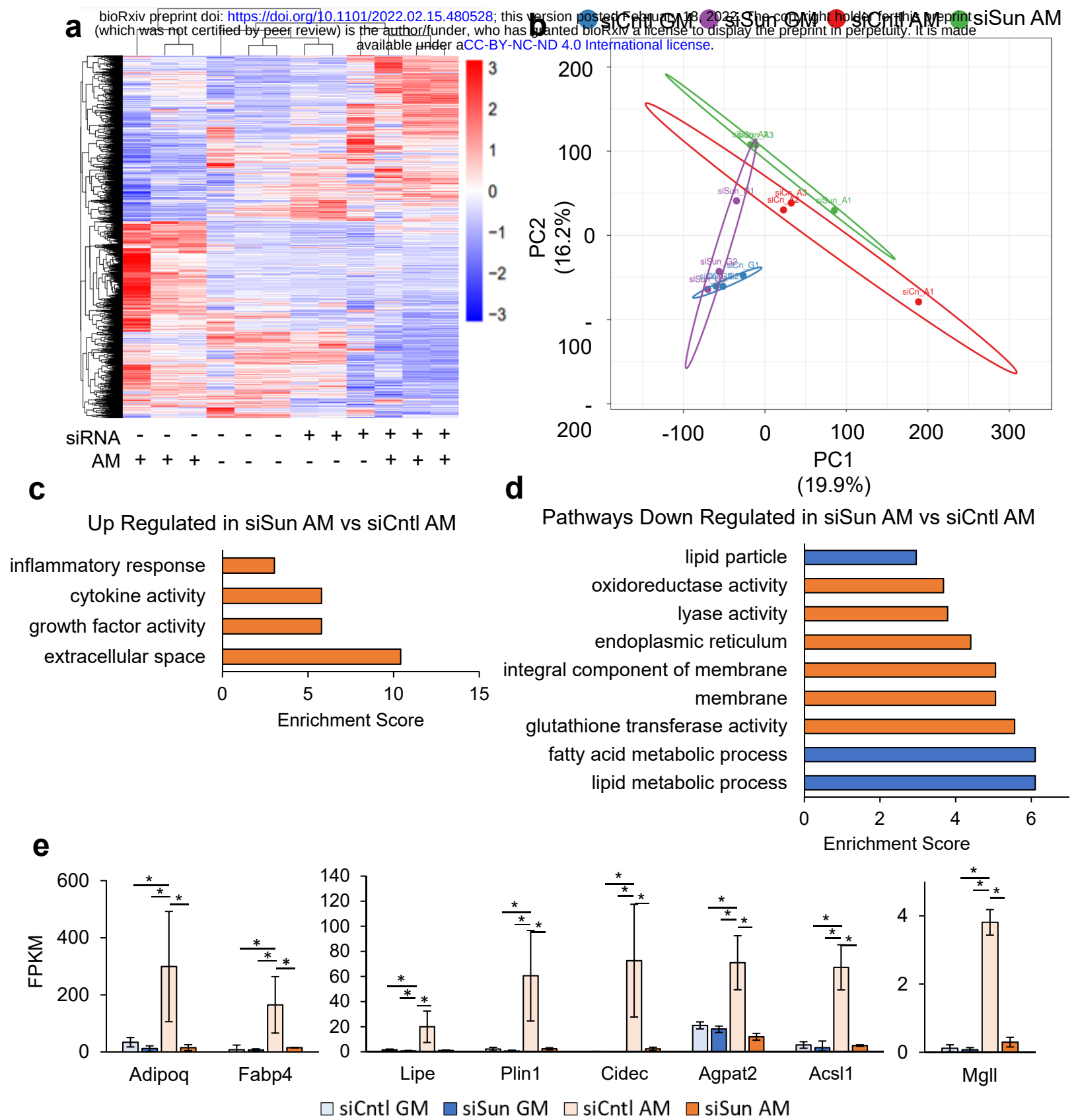

Figure 5: Sun1/2 Depletion Decreases Adipogenesis and Lipid Metabolism Related Genes. **a** Heatmap of genes with significant differential (FC > 1 and P < 0.05) gene expression during Sun1/2 depletion (n = 24). **b** Principle component plot where principal component 1 and principal component 2 explain 19.9% and 16.2% of the total variance, respectively. Prediction ellipses indicate that with a probability of 0.95, a new observation from the same group will fall inside the ellipse. *n* = 24 data points. **c** DAVID analysis of genes up regulated in siSun treatment compared to siCntl. Pathways selected have FDR < 0.05. **d** DAVID analysis of genes down regulated in siSun group compared to siCntl. Pathways selected have FDR < 0.05. Blue indicates pathways related to adipogenesis and lipid metabolism. **e** FPKM values for adipogenic and lipid metabolism related genes detected in both differential gene expression (FC > 1, P < 0.05) and in DAVID analysis (FDR < 0.05) (n = 3/grp). Group comparison was made using One-Way ANOVA where * P < 0.05.

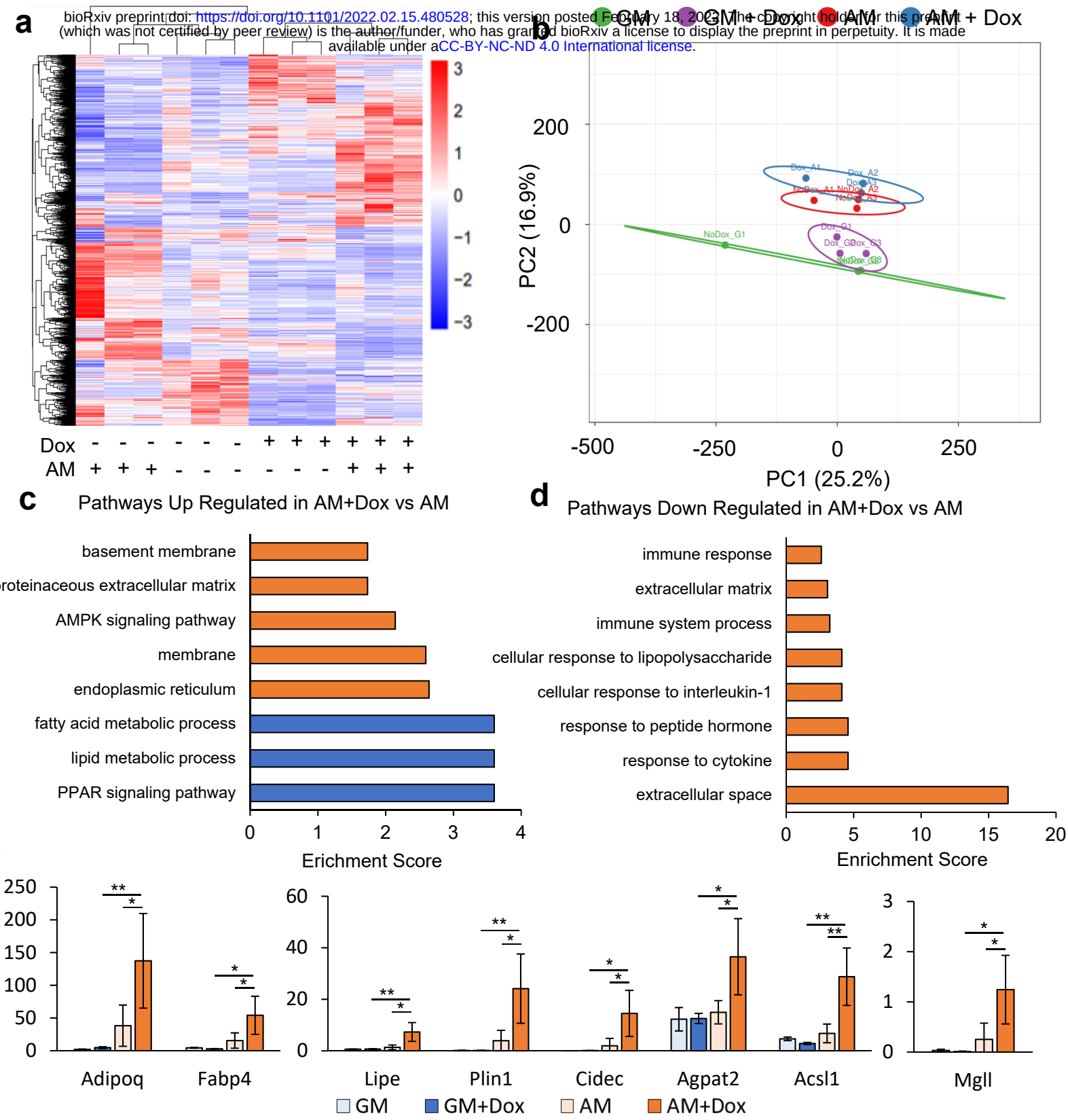

Figure 6: Dominant-Negative KASH Expression Upregulates Adipogenesis Related Pathways. **a** Heatmap of genes with significant differential (FC > 1 and P < 0.05) gene expression during doxycycline induced dnKASH expression (n = 24). **b** Principle component plot where principal component 1 and principal component 2 explain 25.2% and 16.9% of the total variance, respectively. Prediction ellipses indicate that with a probability of 0.95, a new observation from the same group will fall inside the ellipse. *n* = 24 data points. **c** DAVID analysis of genes up regulated in doxycycline treatment compared to control. Blue indicates pathways related to adipogenesis and lipid metabolism. Pathways selected have FDR < 0.05. **d** DAVID analysis of genes down regulated in doxycycline group compared to control. Pathways selected have FDR < 0.05. **e** FPKM values for adipogenic and lipid metabolism related genes detected in both differential gene expression (FC > 1, P < 0.05) and in DAVID analysis (FDR < 0.05) (n = 3/grp). Group comparison was made using One-Way ANOVA. * P < 0.05, ** P < 0.01.

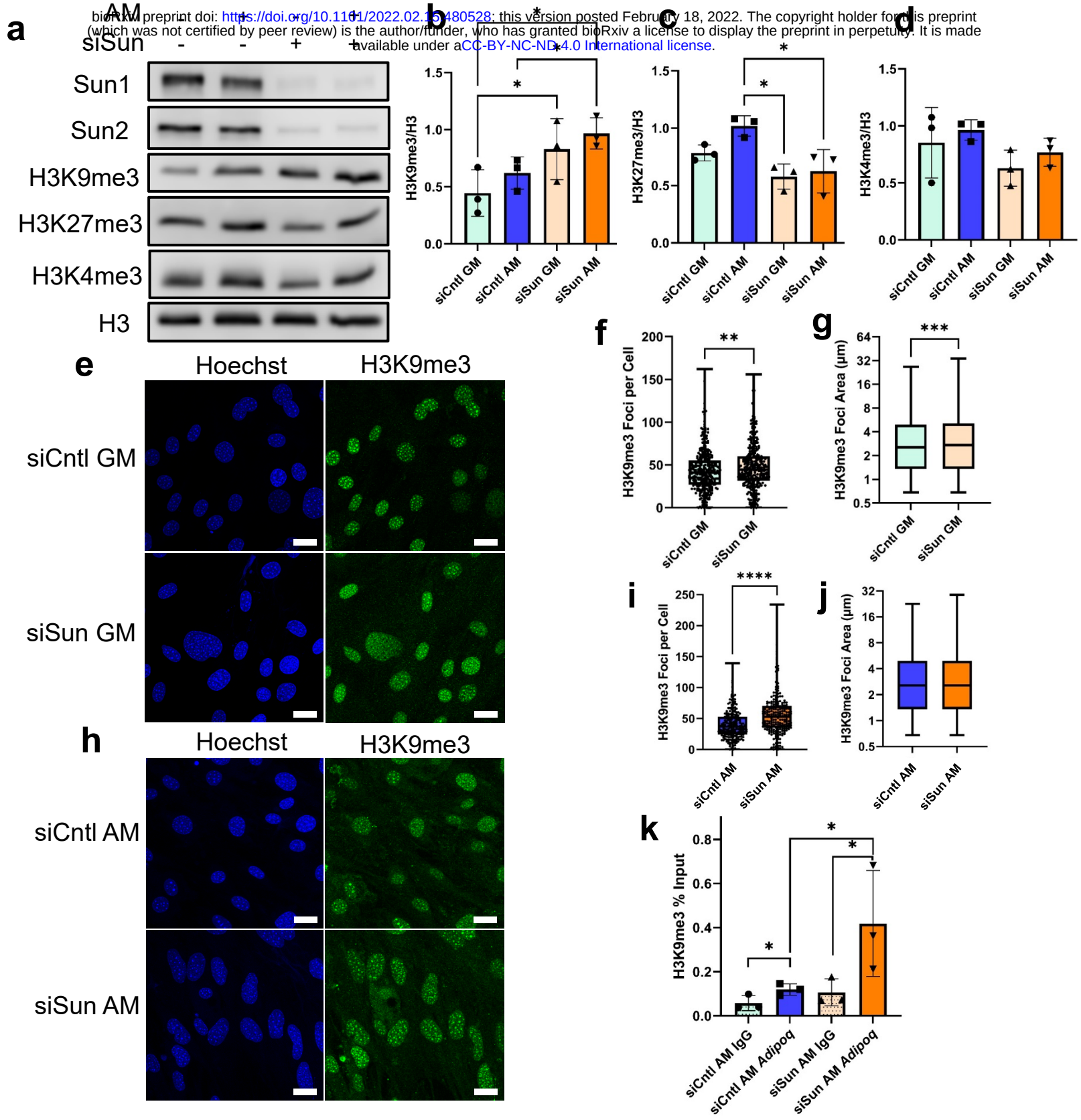

Figure 7: Global levels of H3K9me3 and Enrichment on Adipoq increases during Sun1/2 depletion. **a** Representative western images of heterochromatin markers H3K9me3 and H3K27me3 and euchromatin marker H3K4me3 in siSun and siCntl treatments during growth in growth media and adipogenic media. **b** Western analysis of heterochromatin marker H3K9me3 revealed an increase of 56% in siSun cells compared to siCntl during adipogenesis (n = 3, P < 0.05). **c** H3K27me3 had a decrease of 48% in siSun cells compared to siCntl cells during adipogenesis (n =3, P < 0.05). **d** Euchromatin marker H3K4me3 experienced no significant changes in global protein levels between siSun and siCntl treated cells during adipogenesis. **e** Representative images of siCntl and siSun treated cells grown in growth media staining for H3K9me3 (green) and Hoescht (blue). **f** H3K9me3 foci count per cell in siSun cells compared to siCntl cells in growth media increased by 9% (n = 338, P < 0.01). **g** H3K9me3 foci area increased by 7% in siSun cells compared to siCntl in growth media (n = 14560, P < 0.001). **h** Representative images of siSun and siCntl treated cells grown in adipogenic media and stained for H3K9me3 (green) and Hoechst (blue). **i** H3K9me3 foci count per cell in siSun cell compared to Sicntl Cells during adipogenesis increased by 43% (n = 213, P < 0.0001). **j** No detectable increase of H3K9me3 foci area was found in siSun cells during adipogenesis (n = 8460). **k** CUR&RUN-qPCR targeting H3K9me3 localization on Adipoq showed an increased of 156% in siSun cells compared to siCntl (n = 3, P < 0.05). Western analysis group comparisons were One-Way Anova. H3K9me3 Foci count and area comparisons were made using Mann-Whitney Test. CUR&RUN-qPCR comparisons were done using One-Tailed Students T-Test. * P < 0.05, ** P < 0.01, *** P < 0.001, **** P < 0.0001. Scale bar represents 25µm.

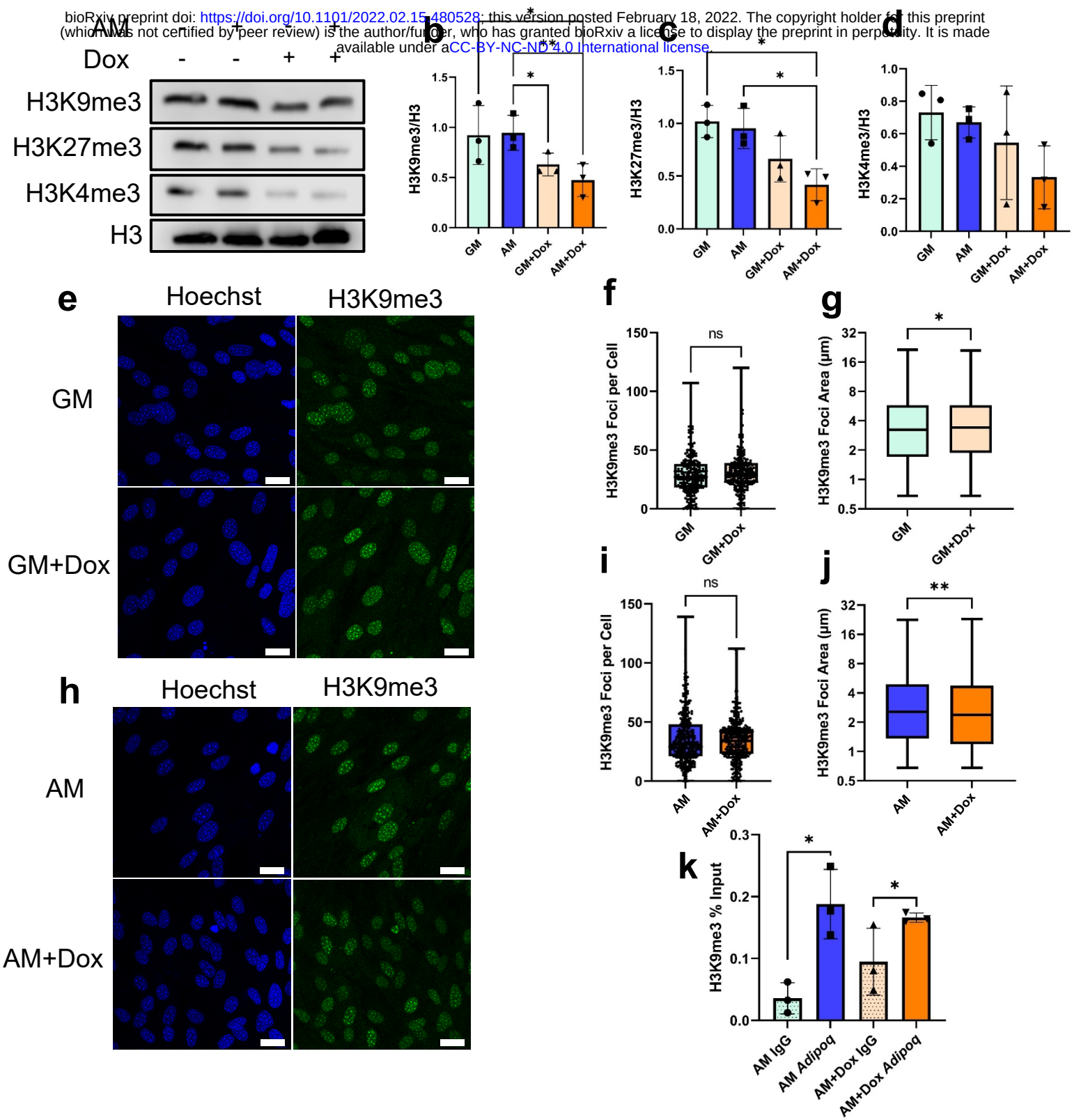

Figure 8: H3K9me3 Levels Are Unaltered During dnKASH Disruption of the LINC Complex. a Representative images of doxycycline induced dnKASH expression of heterochromatin markers H3K9me3 and H3K27me3 and euchromatin marker. **b** H3K9me3 levels decreased during adipogenesis in doxycycline treatment group compared to controls by 51% (n =3, $P < 0.01$). **c** H3K27me3 levels decreased by 56% in doxycycline treatment group compared to control during adipogenesis (n = 3, $P < 0.05$). **d** H3K4me3 levels had no significant changes in doxycycline. **e** Representative confocal imaging of H3K9me3 (green) and DNA (Blue) in growth media. **f** Analysis of H3K9me3 foci count per cell in the doxycycline treatment group in growth media showed no significant changes in foci count per cell (n= 246). **g** H3K9me3 foci area increased by 5% in doxycycline treatment group in growth media (n = 7350, $P < 0.05$). **h** Representative images of doxycycline treated cells and controls cells stained for H3K9me3 (green) and Hoescht (blue) during growth in adipogenic media. **i** H3K9me3 foci count per cell did not show significant changes between doxycycline treatment group and control group during growth in adipogenic media (n = 328). **j** Doxycycline treatment group had decreased H3k9me3 foci area during adipogenesis by 7% compared to control (n = 11317, $P < 0.01$). **k** CUR&RUN-qPCR targeting H3K9me3 localization on Adipoq showed no significant increased in doxycycline treatment cells compared to controls (n = 3). Western analysis group comparisons were One-Way Anova. H3K9me3 Foci count and area comparisons were made using Mann-Whitney Test. CUR&RUN-qPCR comparisons were done using One-Tailed Students T-Test. * $P < 0.05$, ** $P < 0.01$, *** $P < 0.001$, **** $P < 0.0001$. Scale bar represents 25µm.

Supplementary Figures: Depletion of Sun1/2 Induces Heterochromatin Accrual in MSCs during Adipogenesis

Matthew Goelzer[1,4], Sean Howard[1], Anamaria Zavala[1], Daniel Conway[3], Andre J van Wijnen[2], Gunes Uzer[1] †

[1]Boise State University, [2]University of Vermont, [3]Virginia Commonwealth University, [4]Oral Roberts University

† **Corresponding Author**

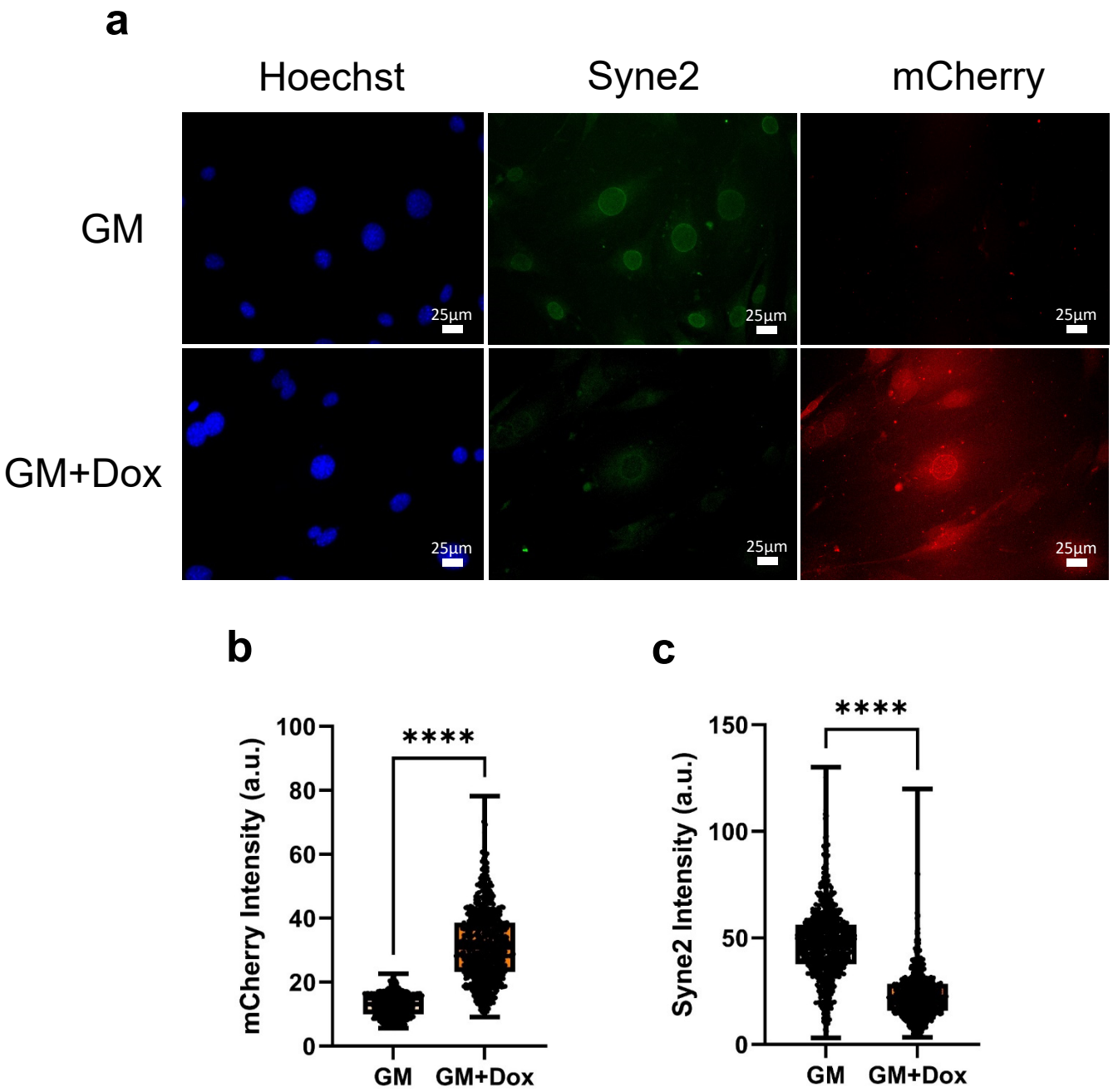

Fig. S1 :dnKASH Expression Displaces Nesprin2 (Syne2) from Nuclear Envelope. a Representative confocal images of nuclei (Hoechst), Syne2 (Green), and dnKASH (mCherry) in GM and GM+Dox treated MSCs. **b** mCherry intensity per nucleus. GM+Dox MSCs had 200% increase of mCherry intensity (n = 1400, P < 0.0001). **c** Nesprin2 (Syne2) inteisty levels per nucleus. GM+Dox cells had 62% decrease in intensity compared to GM group (n – 1400, P < 0.0001). Groups were compared using Two-Tailed Students T-Test where **** = P < 0.0001.

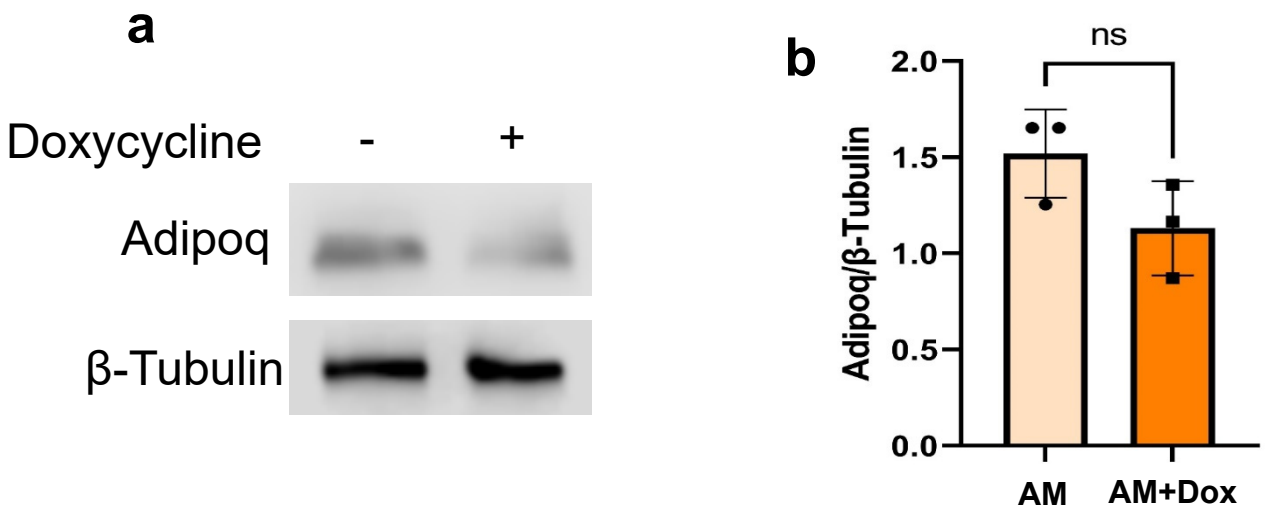

Fig. S2 :Determination of Doxycyline Treatment on Adipogenesis in MSCs. **a** Representative western blot images of Adipoq during growth in adipogenic media with our without doxycycline. **b** Western blot analysis of Adipoq protein levels during in MSCs grown in adipogenic media with and without doxycycline. No significant differences were detected between AM+Dox or AM groups. Groups were compared using Two-Tailed Students T-Test.

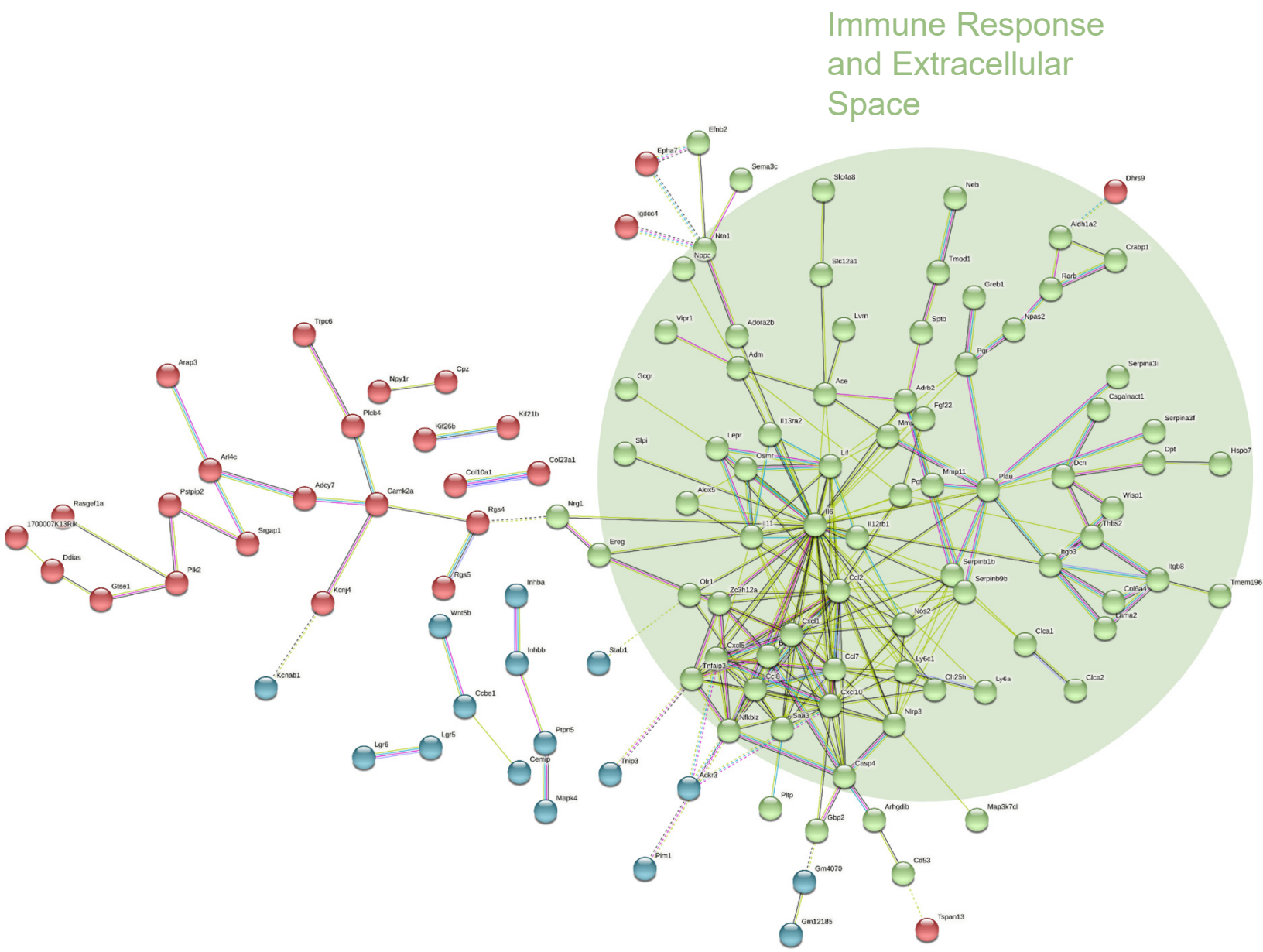

Fig. S3: STRING analysis of up regulated genes in siSun AM vs siCntl AM. Green cluster of genes were associated with immune system response and extracellular space (FDR < 0.05).

Up Regulated Genes in siSun AM vs siCntl AM

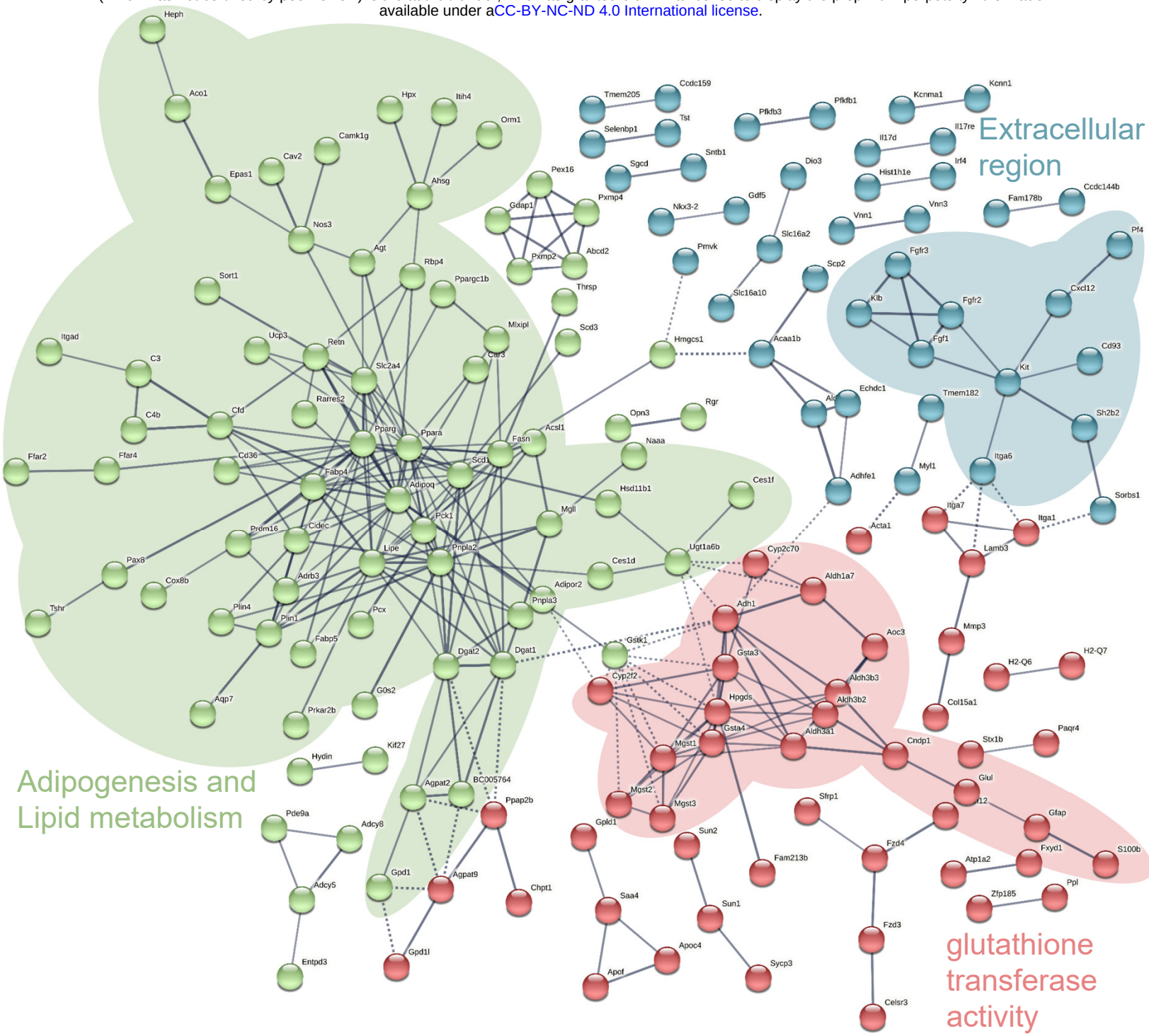

Fig. S4: STRING analysis of down regulated genes in siSun AM vs siCntl AM. Green cluster of genes were associated with adipogenesis and lipid metabolism pathways. Blue cluster represents genes associated with extracellular region. Red cluster identifies genes associated with glutathione transferase activity pathway (FDR < 0.05).

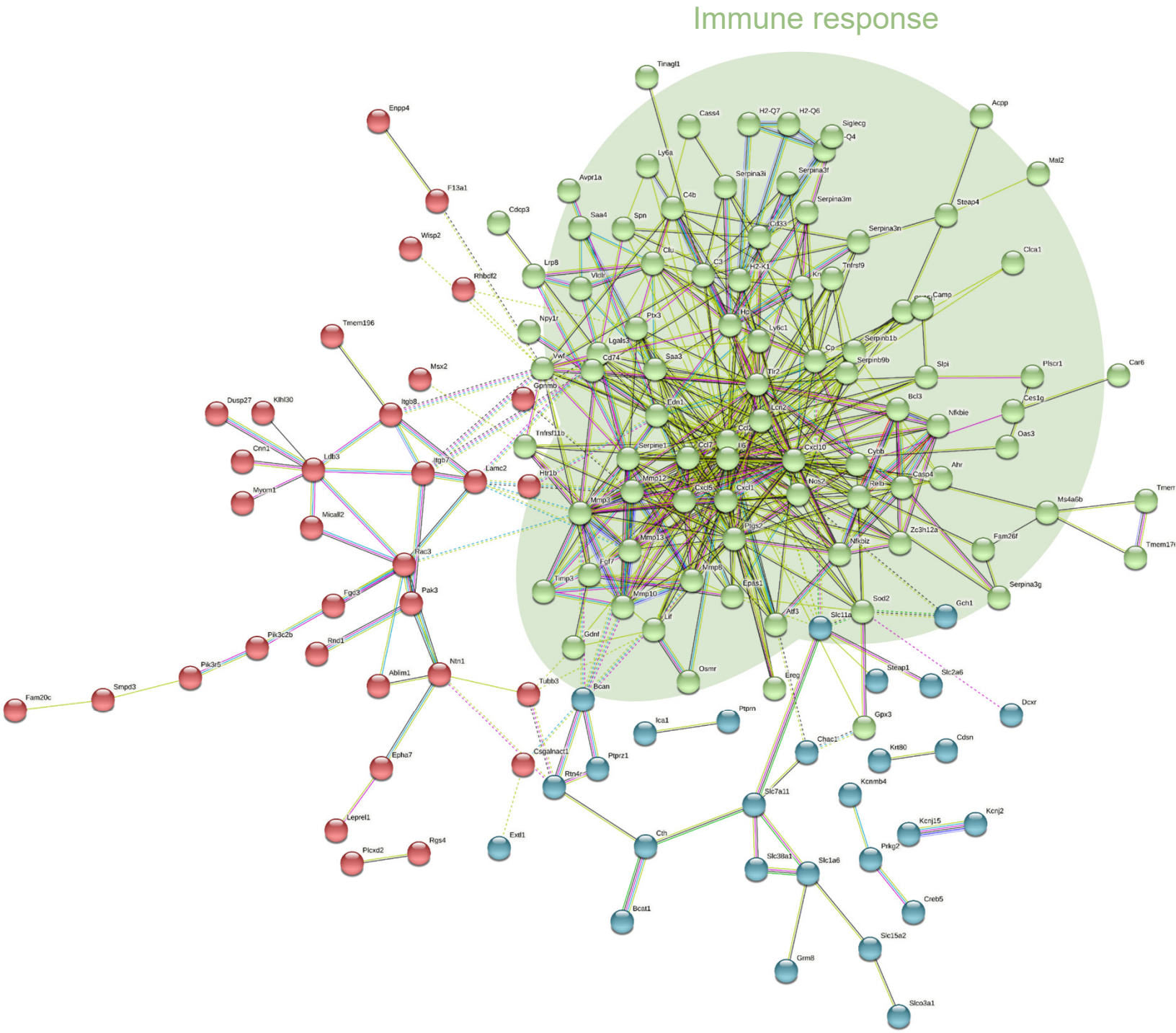

Fig. S5: STRING analysis of down regulated genes in AM+Dox vs AM. Green cluster represents genes identified in immune response pathway (FDR < 0.05).

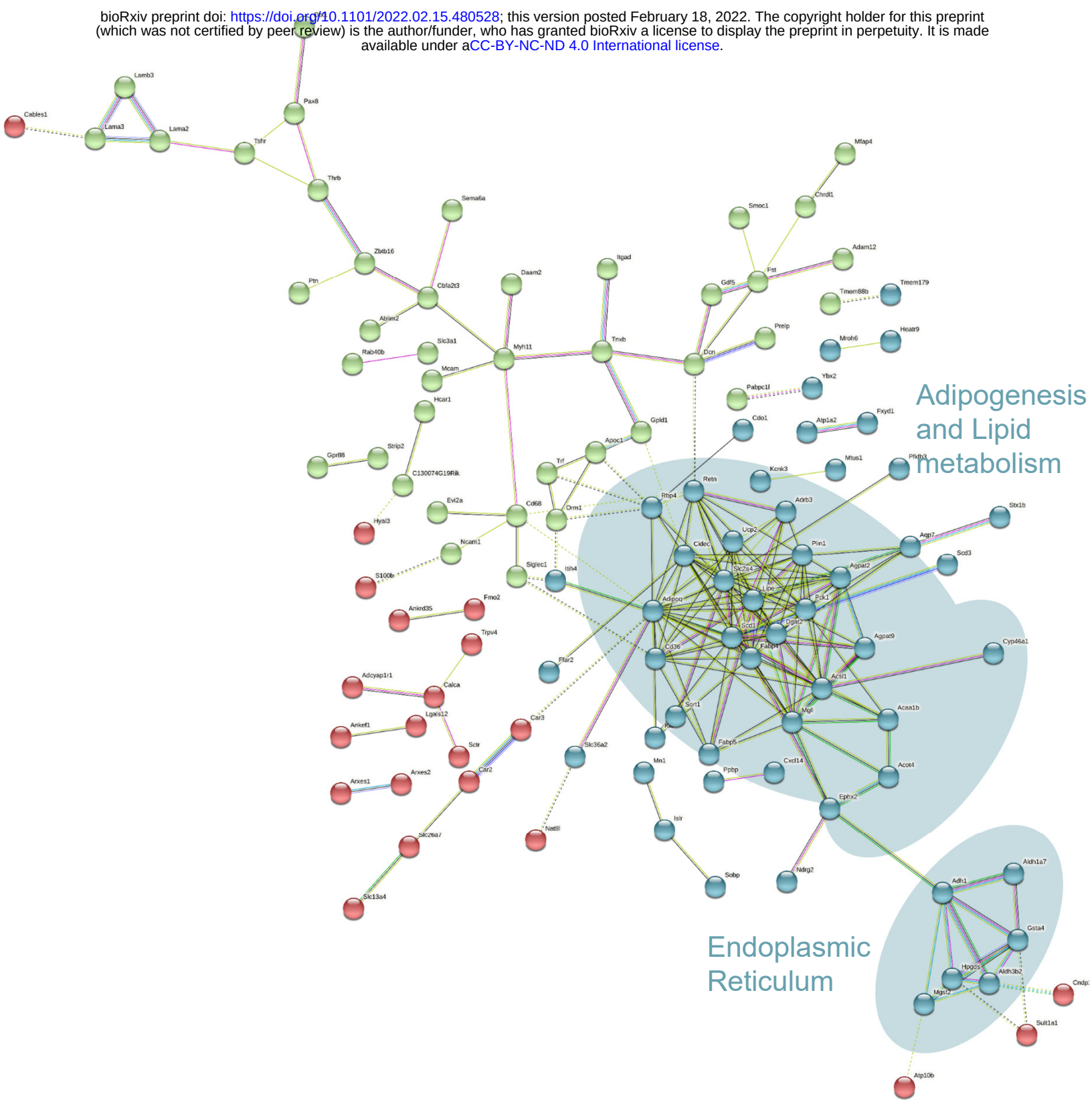

Fig. S6: STRING analysis of up regulated genes in AM+Dox vs AM. Blue cluster of genes were associated with adipogenesis and lipid metabolism pathways and endoplasmic reticulum (FDR < 0.05).

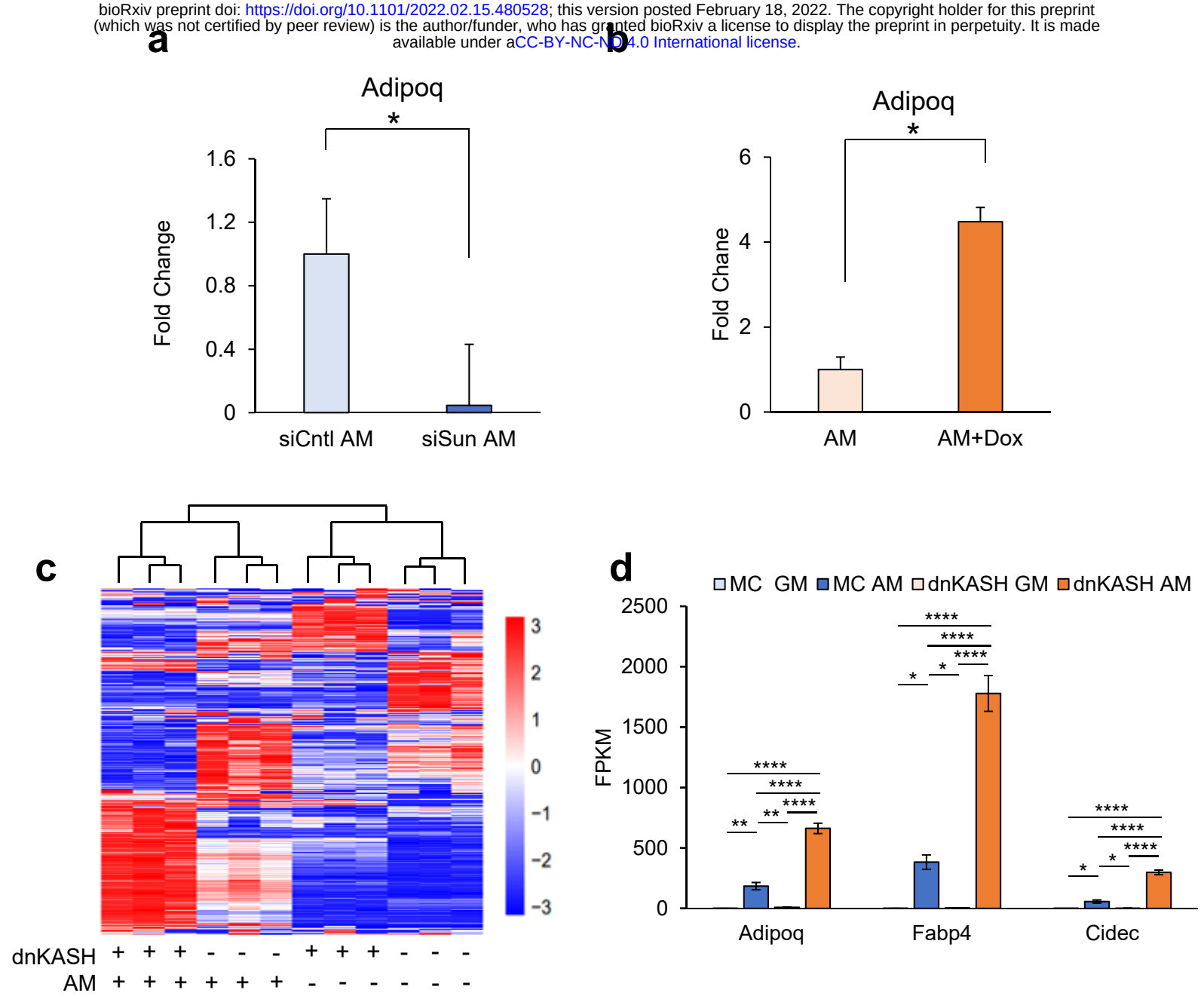

Fig. S7: Validation of siSun and dnKASH Adipogenic Gene Expression. **a** qPCR validation of *Adipoq* levels during growth in AM and siSun treatment. *Adipoq* expression decreased by 90% (n = 3, P < 0.05). **b** qPCR validation of Adipoq levels during growth in AM or AM+Dox media. *Adipoq* expression in dnKASH expressing MSCs had 4-fold increase of Adipoq expression (n = 3, P < 0.05). **c** Heatmap of MSCs transfected with secondary plasmid expressing dnKASH or empty vector (MC) during growth in GM or AM media. Genes selected had FPKM > 0.3 and P < 0.05 compared to controls. **d** FPKM levels of *Adipoq, Fabp4,* and *Cidec* during transfection with either dnKASH or MC in GM or AM media. *Adipoq, Fabp4,* and *Cidec* experienced increases of 280% (n =3, P < 0.0001), 400% (n =3, P < 0.0001), and 500% (n =3, P < 0.0001), respectively, in FPKM levels between MC AM and dnKASH AM groups. qPCR validation of siSun and dnKASH Groups were compared using Two-Tailed Students T-Test. FPKM analysis of adipogenic genes *Adipoq, Fabp4,* and *Cidec* was done by One-Way Anova. * P < 0.05, ** P < 0.01, *** P < 0.001, **** P < 0.0001.

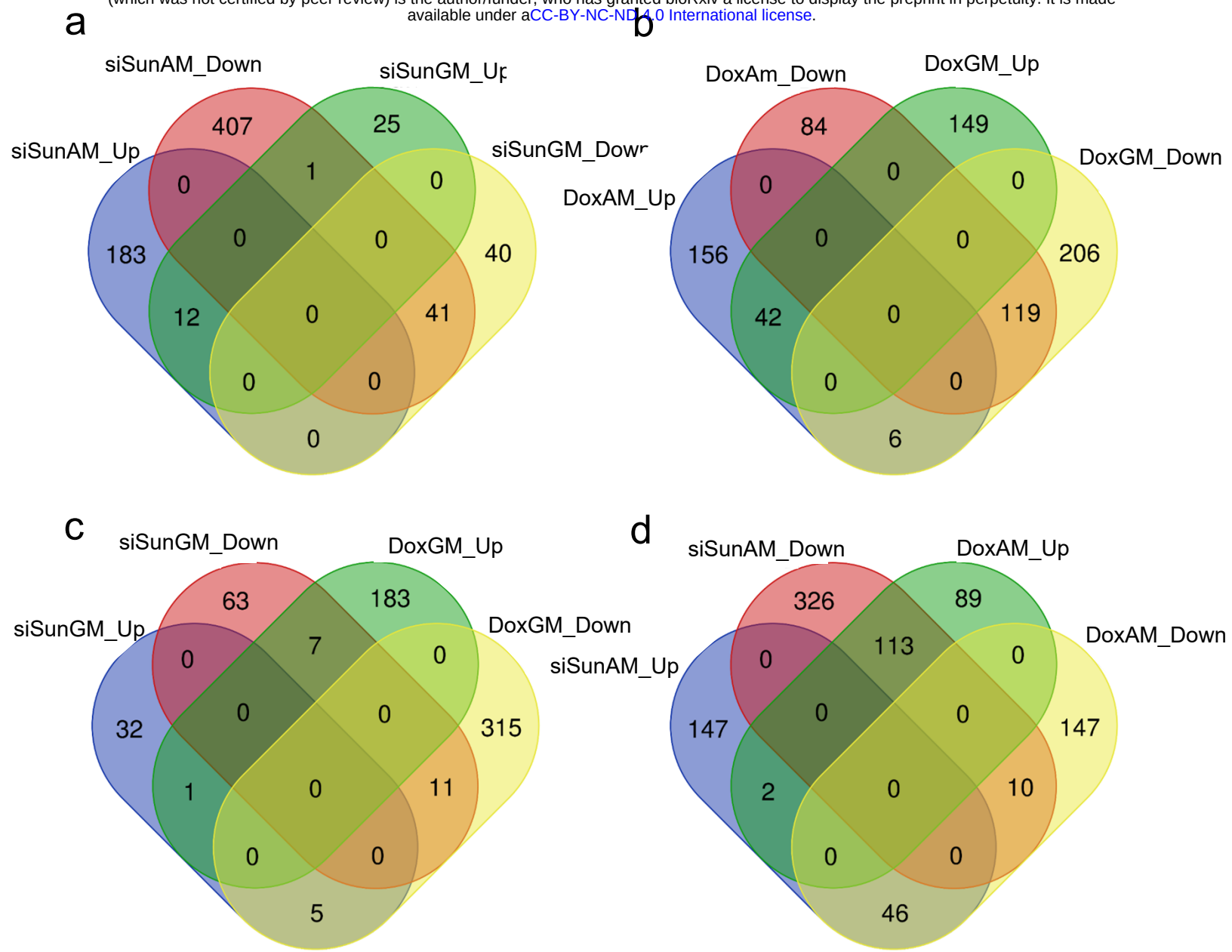

Fig. S4: Venn Diagrams of RNA-Seq Analysis. a Venn diagram depicting gene expression overlap for genes up or down regulated in siSun compared to siCntl during growth in GM or AM. **b** Venn diagram depicting gene expression overlap for genes up or down regulated in GM+Dox or AM+Dox compared to GM or AM respectivly. **c** Comparrison of siSun GM up and down regulated genes compared to siCntl GM and GM+Dox up and down regulated genes compared to GM. **d** Comparrison of siSun AM up and down regulated genes compared to siCntl AM and AM+Dox up and down regulated genes compared to AM.

Table S1. DAVID analysis of genes up regulated in siSun AM vs siCntl AM comparison.

Term	PValue	Genes	FDR
Enrichment Score: 10.410501090574954			
GO:0005576~extracellular region	6.54E-13	ADM, CXCL1, CPZ, WISP1, CXCL5, FCNA, NPPC, PRL2C3, PLAU, CASP4, LEPR, COL10A1, OLR1, IL13RA2, CCBE1, IL11, WNT5B, ANG2, COL23A1, NRG1, PGF, DCN, EREG, MMP11, SLPI, COL6A4, FAM20C, APOL7A, CEMIP, LAMA2, SEMA3C, SAA3, DPT, THBS2, NTN1, PRRG4, CCL8, CCL7, CCL2, NLRP3, PLTP, FGF22, CTLA2A, ACE, BMP8A, LIF, INHBB, INHBA, CXCL10, IL6	1.16E-10
GO:0005615~extracellular space	6.37E-10	SEMA3C, SAA3, DPT, ADM, CXCL1, CPZ, CST6, CXCL5, NPPC, SERPINB1B, PRL2C3, CCL8, SERPINA3F, CCL7, PLAU, ALOX5, LEPR, CCL2, SERPINB9B, PLTP, CCBE1, IL11, ACE, NOS2, WNT5B, COL23A1, BMP8A, LIF, INHBB, NRG1, INHBA, PGF, SERPINA3I, DCN, EREG, CXCL10, CES1A, IL6, PPFIBP2, SLPI, FAM20C	5.67E-08
Enrichment Score: 5.786565731582282			
GO:0008083~growth factor activity	8.07E-07	IL11, IL6, PRL2C3, BMP8A, LIF, INHBB, CXCL1, INHBA, FGF22, PGF, EREG	2.66E-04
GO:0005125~cytokine activity	4.07E-06	CXCL10, IL11, IL6, CCL8, CCL7, BMP8A, LIF, CCL2, INHBB, CXCL1, INHBA, CXCL5	6.72E-04
Enrichment Score: 3.036176147602188			
GO:0006954~inflammatory response	6.80E-07	NOS2, TNFAIP3, CXCL1, CXCL5, CXCL10, IL6, CCL8, CCL7, ALOX5, CASP4, ZC3H12A, STAB1, NFKBIZ, CCL2, OLR1, NLRP3	7.89E-04
GO:0005125~cytokine activity	4.07E-06	CXCL10, IL11, IL6, CCL8, CCL7, BMP8A, LIF, CCL2, INHBB, CXCL1, INHBA, CXCL5	6.72E-04
GO:0070098~chemokine-mediated signaling pathway	1.09E-05	CXCL10, CCL8, CCL7, CCL2, ACKR3, CXCL1, CXCL5	0.004225
GO:0008009~chemokine activity	7.15E-05	CXCL10, CCL8, CCL7, CCL2, CXCL1, CXCL5	0.007866

Table S2. DAVID analysis of genes down regulated in siSun AM vs siCntl AM comparison.

Term	PValue	Genes	FDR
Enrichment Score: 6.524333497927802			
GO:0005615~extracellular space	2.35903E-06	ORM1, COL14A1, TRF, FGF1, DMKN, PCSK4, C4B, THBD, NAT8F3, LIPE, LBP, CD36, EGFL7, WFDC21, IGFBP4, AHSG, RALGAPA2, ADIPOQ, MMP3, MTUS1, CES4A, ALDH3A1, ACTA1, SFRP1, RBP4, TST, NRG4, KIT, SPARCL1, AMY1, GAS6, GPLD1, S100A8, CFD, COL15A1, LYZ2, SAA4, SEMA3G, STC1, RETN, C3, SERPINA3C, SELENBP1, HPX, AOC3, CAR2, S100B, GDF5, AGT, APLN, VNN1, CXCL12, LRG1, PPP1R1A, CES1D, VNN3, CES1F, LCN2, MDGA1, PF4	0.000131
GO:0005576~extracellular region	0.000112746	SNED1, ORM1, COL14A1, TRF, FGF1, DMKN, CHRDL1, WFDC3, C4B, ESM1, LBP, EGFL7, WFDC21, IGFBP4, AHSG, ADIPOQ, MMP3, IL17RE, OTOR, CES4A, FNDC5, SFRP1, RBP4, OLFM2, NRG4, SPARCL1, AMY1, IGFALS, GAS6, MATN4, GPLD1, S100A8, CFD, ITIH4, COL15A1, MEGF6, LYZ2, SAA4, SEMA3G, STC1, RETN, C3, SERPINA3C, HPX, PRRG1, APOF, LAMB3, RARRES2, APOC4, S100B, GDF5, KAZALD1, ABHD15, CXCL12, SMOC1, LCN2, SIGLEC1, IL17D, FGFR2, PF4, CBLN1	0.003483
Enrichment Score: 6.1042355089644165			
GO:0006629~lipid metabolic process	1.32922E-11	GAL3ST1, PCX, FAM57B, GDPD2, ACAA1B, CYP46A1, ADIPOR2, AGPAT2, SULT1A1, C3, HSD11B1, LIPE, HPGDS, FAM213B, SPTLC3, PMVK, APOF, SCD3, SCD1, PCK1, DGAT2, HMGCS1, ACSL1, FA2H, FABP5, CES1D, FASN, NAAA, PNPLA3, ECHDC2, THRSP, CHPT1, PLIN1, PPARA, PLCB2, MGLL, PNPLA2	1.33E-08
GO:0006631~fatty acid metabolic process	2.07319E-07	ACSL1, ACAA1B, ADIPOR2, C3, FA2H, HPGDS, FAM213B, FABP4, PRKAR2B, UCP3, FASN, SCD3, ECHDC2, CD36, SCD1, PPARA, MGLL	0.000104
Enrichment Score: 5.559184156465526			
GO:0004364~glutathione transferase activity	4.84182E-06	GSTK1, HPGDS, GSTA4, GSTA3, MGST3, MGST1, MGST2, GDAP1	0.003162
Enrichment Score: 5.054084638725923			
GO:0016020~membrane	2.48959E-08	CLEC10A, AQP7, KLHDC7A, FGFRL1, ZFYVE28, LIPE, SCP2, CYP2C70, GBP6, PAQR9, GSTK1, PAQR4, UNC5A, ACSL1, MTUS1, MCEMP1, MFSD12, GBGT1, TMEM82, FNDC5, SLC5A6, STX1B, RNF125, KCNQ4, PLPP3, SLC22A4, SLC22A3, ADCYAP1R1, MGST3, MGST1, APCDD1, PPL, SLC5A3, HSD11B1, MC2R, PRKAR2B, KCNN1, RHBDL3, FZD3, FZD4, ABCA9, SLC16A10, GDF5, FA2H, VNN1, VNN3, FASN, FXYD1, HIST1H4H, TMCC3, IFI27L2A, A530016L24RIK, FAM57B, TMEM182, PCSK4, RYR3, PHEX, VSIR, PANX2, SPTLC3, B3GALT2, SLC22A18, TMED3, FFAR4, SCD3, FFAR2, CD36, SCD1, SLC18A1, ADIG, COX8B, CHST7, IL17RE, TMEM179, ADRB3, KCNMA1, KIT, PLIN4, TLR8, RGR, SLC22A20, MGLL, PLPPR3, PTGER3, TXLNG, GDPD2, FITM2, ADCY8, BEGAIN, ADCY5, UCP3, CYP2F2, PEX16, AOC3, CAR2, SORT1, SCTR, FMO1, SORBS1, LHFPL1, MC5R, PNPLA3, SIGLEC1, PNPLA2, KLB, SCARB1, CLSTN3, CYP46A1, CELSR3, MPC2, ADORA1, SLC16A9, SLC16A2, DGAT2, SLC15A2, DGAT1, CD93, ABCA8A, SEMA6D, DIO3, OLFM2, ADAM12, LY6H, PDE9A, DSC2, S100A8, RTN4R, RASGRP2, ADIPOR2, ALDH3B3, HCAR2, HCAR1, PMVK, CD300LG, TMEM120B, OPN3, BTN2A2, CAV2, TMEM120A, GFAP, ABHD15, PXMP2, PXMP4, REEP6, FGFR3, FGFR2, TMEM45B, ABCD2, GAL3ST1, TRF, SLC2A4, TSPAN12, RERG, THBD, CD1D1, SGCD, HEPH, GPER1, ADGRE4, LBP, SUN2, SUN1, SVOP, SLC36A2, ITGA1, ARL4A, ITGAD, IRF4, NRG4, ITGA7, ITGA6, SLC25A10, NAT8L, CAMK1G, H2-Q6, H2-Q7, ATP1A2, AGPAT2, SELENBP1, CNNM1, RAB40B, RASD1, TMEM205, LRRC8D, RILP, SH2B2, NOS3, KCNIP3, SPRY4, ATP2B4, C130074G19RIK, GDAP1, TSHR, P2RX6, CHPT1, GPD1L, PIK3AP1, SLC25A34, MDGA1, KCNK3, SNTB1, CBLN1	6.92E-06
GO:0016021~integral component of membrane	0.002647796	KLB, SCARB1, GM5460, CLSTN3, CLEC10A, AQP7, KLHDC7A, ARXES2, ARXES1, CYP46A1, CELSR3, FGFRL1, MFSD13B, MPC2, ADORA1, SLC16A9, SLC16A2, PAQR9, SLC15A2, DGAT2, DGAT1, ENTPD3, CD93, ABCA8A, UNC5A, PAQR4, ACSL1, SEMA6D, MTUS1, DIO3, MCEMP1, MFSD12, GBGT1, TMEM82, FNDC5, SLC5A6, ALDH3A1, STX1B, SFRP1, ADAM12, KCNQ4, PLPP3, DSC2, SLC22A4, SLC22A3, ADCYAP1R1, MGST3, MGST1, MGST2, APCDD1, ADIPOR2, SLC5A3, HSD11B1, HCAR2, MC2R, HCAR1, KCNN1, RHBDL3, CD300LG, TMEM120B, FZD3, OPN3, BTN2A2, FZD4, CAV2, TMEM120A, ABCA9, SLC16A10, FA2H, VNN1, PXMP2, FXYD1, TMCC3, PXMP4, REEP6, IFI27L2A, FGFR3, FGFR2, TMEM45B, ABCD2, GAL3ST1, A530016L24RIK, FAM57B, TMEM182, SLC2A4, TSPAN12, VSIR, RYR3, PHEX, THBD, PANX2, NAT8F3, CD1D1, SGCD, HEPH, SPTLC3, GPER1, SLC22A18, B3GALT2, ADGRE4, TMED3, FFAR4, SCD3, FFAR2, SCD1, CD36, SLC18A1, ADIG, SUN2, NXPE5, SUN1, SLC36A2, SLC13A4, SVOP, COX8B, CHST7, GM10134, ITGA1, IL17RE, UGT1A6B, TMEM179, ADRB3, ITGAD, NRG4, KCNMA1, KIT, ITGA7, TLR8, ITGA6, SLC25A10, NAT8L, RGR, SLC22A20, PLPPR3, H2-Q6, PTGER3, H2-Q7, GDPD2, ATP1A2, FITM2, LRP3, ADCY8, AGPAT2, ADCY5, CNNM1, TMEM205, UCP3, PRRG1, VMN2R57, LRRC8D, GPR155, PEX16, AOC3, POLN, SORT1, ATP2B4, C130074G19RIK, SCTR, G0S2, FMO1, LHFPL1, FAM213A, GDAP1, TSHR, P2RX6, MC5R, PNPLA3, GM11127, CHPT1, SIGLEC1, SLC25A34, KCNK3, PNPLA2	0.043299
Enrichment Score: 4.400392717334829			
GO:0005783~endoplasmic reticulum	9.42399E-07	CLSTN3, FAM57B, ARXES2, ARXES1, CYP46A1, RYR3, PHEX, NAT8F3, SCP2, SPTLC3, GPER1, ADORA1, TMED3, SCD3, SCD1, CYP2C70, CD36, MAP3K5, DGAT2, DGAT1, ACSL1, ADIPOQ, UGT1A6B, FNDC5, ALDH3A1, KCNMA1, PLIN1, PLPP3, NAT8L, PDE9A, RTN4R, MGST3, H2-Q6, H2-Q7, MGST1, OAS1A, MGST2, FITM2, AGPAT2, HSD11B1, FAM213B, LRRC8D, CYP2F2, PEX16, AOC3, SORT1, CAV2, KCNIP3, FMO1, CIDEC, FA2H, CES1D, CES1F, ACO1, REEP6, FGFR3	7.7E-05
Enrichment Score: 3.786951718342054			
GO:0016829~lyase activity	4.11812E-05	CAR3, CAR2, CAR1, THA1, ADCY8, ADCY5, CAR5B, FASN, ECHDC1, ECHDC2, ACO1, PCK1, GLUL	0.013446
Enrichment Score: 3.677802891089701			
GO:0016491~oxidoreductase activity	0.000230652	CYP46A1, DHTKD1, PRDX3, ALDH3B3, HSD11B1, ALDH3B2, ADH1, FAM213B, HEPH, SCD3, SCD1, CYP2F2, CYP2C70, PRODH, AOC3, NOS3, ADHFE1, DIO3, FMO1, HPDL, ALDH3A1, FA2H, ALDH6A1, FASN, GPD1, GPD1L, CDO1, ALDH1A7	0.037654
Enrichment Score: 2.958793657193554			
GO:0005811~lipid particle	1.10822E-06	ALDH3B2, LIPE, DGAT2, CES1D, CAV2, CES1F, PNPLA3, PLIN4, PLIN1, CIDEC, PNPLA2	7.7E-05
Enrichment Score: 2.9194437076370603			
GO:0005778~peroxisomal membrane	0.000825684	FNDC5, PEX16, ABCD2, ACSL1, PXMP2, MGST1, PXMP4	0.015871
GO:0005777~peroxisome	0.001811594	FNDC5, PEX16, GSTK1, ABCD2, SCP2, ACSL1, PXMP2, PMVK, PXMP4, ACAA1B	0.031476
Enrichment Score: 2.783046834549974			
GO:0004364~glutathione transferase activity	4.84182E-06	GSTK1, HPGDS, GSTA4, GSTA3, MGST3, MGST1, MGST2, GDAP1	0.003162
Enrichment Score: 1.9621782871517306			
GO:0004364~glutathione transferase activity	4.84182E-06	GSTK1, HPGDS, GSTA4, GSTA3, MGST3, MGST1, MGST2, GDAP1	0.003162
Enrichment Score: 0.7843121871123002			
GO:0031090~organelle membrane	0.000160598	FA2H, MGST3, SCD3, FMO1, ARXES2, CYP2F2, SCD1, ARXES1, CYP2C70, CYP46A1	0.004189

Table S9. DAVID analysis of genes up-regulated in AM vs AM+Dox comparison.

Term	PValue	Genes	FDR
Enrichment Score: 5.164491013153225			
GO:0005576~extracellular region	1.55E-05	ITIH4, CALCA, ORM1, TNXB, LAMA2, NXPH3, LAMA3, TRF, PRELP, PTN, RETN, CXCL14, CHRDL1, TMEM25, ISLR, ADGRG1, PDZD2, HYAL3, LAMB3, FST, ADIPOQ, IL17RE, S100B, GDF5, DCN, ABHD15, MFAP4, RBP4, OLFM2, CRISPLD1, CRISPLD2, SMOC1, APOC1, VWA1, SIGLEC1, GPLD1	0.00267
Enrichment Score: 3.6014436708635866			
mmu03320:PPAR signaling pathway	3.36E-08	FABP4, FABP5, ACSL1, ADIPOQ, SCD3, AQP7, ACAA1B, PLIN1, SCD1, CD36, PCK1	4.26E-06
GO:0006629~lipid metabolic process	5.74E-07	TNXB, DGAT2, HPGD, ACSL1, EPHX2, ACAA1B, CYP46A1, AGPAT2, SULT1A1, LIPE, HPGDS, FABP5, SPTLC3, SCD3, PLIN1, PLCH2, SCD1, PCK1, MGLL	4.48E-04
GO:0006631~fatty acid metabolic process	2.24E-05	HPGDS, TNXB, FABP4, HPGD, ACSL1, SCD3, ACAA1B, SCD1, CD36, MGLL	0.007989
Enrichment Score: 2.6399772091369966			
GO:0005783~endoplasmic reticulum	6.70E-04	MOXD1, CALR3, MGST2, ATP10B, ARXES2, PTN, ARXES1, CYP46A1, AGPAT2, PDZD2, SPTLC3, SCD3, LRRC8D, CD36, SCD1, MEST, DGAT2, ACSL1, SORT1, ADIPOQ, FMO2, CIDEC, APOC1, PLIN1, REEP6, NAT8L	0.028823
Enrichment Score: 2.591431031118175			
GO:0016020~membrane	8.58E-04	KLB, MOXD1, A530016L24RIK, TENM4, DOCK8, SLC40A1, TRF, AQP7, CIB2, TMEM182, KLHDC7A, SLC2A4, CYP46A1, LIPE, SPTLC3, B3GALT2, SCD3, FFAR2, SCD1, CD36, GAL3ST2, PAQR9, TMEM88B, SEMA6A, SLC36A2, DGAT2, ABCA8A, ACSL1, SEMA6D, MTUS1, IL17RE, CBFA2T3, GBGT1, STX1B, TMEFF2, TMEM179, ARC, OLFM2, ADRB3, ITGAD, ADGRB2, RGS9BP, ADAM12, MYZAP, NAT8L, GPRC5C, MGLL, ADCYAP1R1, C5AR2, PTGER3, GPR88, WNK4, SLC3A1, ATP1A2, PTN, APCDD1, AGPAT2, TMEM25, SELENBP1, ADGRG1, MC2R, RAB40B, HCAR1, UCP2, LRRC8D, NCAM1, MEST, CD300LG, CAR2, SORT1, MCAM, PTCH2, C130074G19RIK, SCTR, FMO2, GDF5, TSHR, ABHD15, TRPV4, FXYD1, TMCC3, SLC26A7, SIGLEC1, PLCH2, REEP6, SLC25A34, CD68, KCNK3	0.029507
Enrichment Score: 2.1409380701327043			
mmu04152:AMPK signaling pathway	8.68E-04	LIPE, PFKFB3, ADIPOQ, SCD3, SLC2A4, SCD1, CD36, PCK1	0.036734
Enrichment Score: 1.7324571669713142			
GO:0005578~proteinaceous extracellular matrix	2.09E-04	MFAP4, TNXB, LAMA2, LAMB3, CRISPLD2, SMOC1, LAMA3, VWA1, PRELP, PTN, GPLD1, DCN	0.017839
GO:0005604~basement membrane	3.11E-04	LAMA2, LAMB3, SMOC1, LAMA3, VWA1, TRF, PTN	0.017839

Table S4. DAVID analysis of genes down regulated in AM vs AM+Dex comparison.

Term	PValue	Genes	FDR
Enrichment Score: 16.442538003224215			
Term	PValue	Genes	FDR
GO:0005615~extracellular space	1.6417017461634274E-21	TINAGL1, SERPINE1, HP, LAMC2, CXCL1, VLDLR, CLU, CXCL5, WISP2, SPN, C4B, LGALS3, FGF7, TIMP3, CAR6, LMCD1, CAMP, CCBE1, EDN1, VWF, GPX3, MMP3, MMP8, EREG, BCAN, MMP13, SLPI, OAS3, FAM20C, ACPP, SAA3, SAA4, TNFRSF11B, LTBP2, LRP8, KNG1, RNASET2A, C3, SERPINB1B, SERPINA3F, CCL7, PTPRZ1, STC2, CCL2, SERPINB9B, NOS2, TNFRSF9, LIF, SERPINA3M, SERPINA3N, SERPINA3G, CP, SERPINA3I, CXCL10, IL6, GDNF, CES1G, CLEC2G, LCN2, PTX3	3.2013184050186834E-19
GO:0005576~extracellular region	5.692614007016396E-17	TINAGL1, SERPINE1, HP, F13A1, LAMC2, CXCL1, ISM1, CLU, CXCL5, WISP2, C4B, LGALS3, FGF7, CASP4, TIMP3, CAR6, CAMP, CCBE1, EDN1, VWF, GPX3, MMP3, MMP8, MMP10, EREG, MMP12, BCAN, MMP13, SLPI, ANGPTL6, FAM20C, VSTM2A, ACPP, SAA3, SAA4, TNFRSF11B, LTBP2, NTN1, LRP8, KNG1, 5430419D17RIK, C3, CCL7, PTPRZ1, STC2, CCL2, CDSN, LIF, SERPINA3M, SERPINA3N, CP, CXCL10, IL6, GDNF, LCN2, PTX3, NOTUM, HPSE	5.5502986568409865E-15
Enrichment Score: 4.585972071952109			
Term	PValue	Genes	FDR
GO:0034097~response to cytokine	1.8576718254593303E-5	SERPINA3F, SERPINA3M, SERPINA3N, PTGS2, SERPINA3G, OSMR, SERPINA3I, RELB	0.004102358614556021
GO:0010466~negative regulation of peptidase activity	2.6176895538567044E-5	SERPINB1B, SERPINA3F, SLPI, SERPINE1, TIMP3, SERPINA3M, SERPINA3N, SERPINA3G, KNG1	0.004336764545185795
GO:0004867~serine-type endopeptidase inhibitor activity	3.239574315699336E-5	SERPINB1B, SERPINA3F, SLPI, SERPINE1, SERPINB9B, SERPINA3M, SERPINA3N, SERPINA3G, SERPINA3I	0.006398159273506189
GO:0030414~peptidase inhibitor activity	3.239574315699336E-5	SERPINB1B, SERPINA3F, SLPI, SERPINE1, TIMP3, SERPINA3M, SERPINA3N, SERPINA3G, KNG1	0.006398159273506189
GO:0043434~response to peptide hormone	9.897662481969958E-5	SERPINA3F, STC2, SERPINA3M, SERPINA3N, SERPINA3G, SERPINA3I, EREG	0.013114402788610195
Enrichment Score: 4.127262509244919			
Term	PValue	Genes	FDR
GO:0071347~cellular response to interleukin-1	1.531896347360444E-6	IL6, EDN1, CCL7, SAA3, ZC3H12A, SERPINE1, LCN2, CCL2, CAMP	6.765875534175294E-4
GO:0071222~cellular response to lipopolysaccharide	2.966452906842876E-4	CXCL10, IL6, PLSCR1, NOS2, PLSCR2, ZC3H12A, SERPINE1, LCN2, CCL2, CAMP	0.03275458417972343
Enrichment Score: 3.2278474521875653			
Term	PValue	Genes	FDR
GO:0002376~immune system process	1.5545629792378633E-4	CD74, H2-Q7, H2-K1, HP, AHR, SERPINA3G, C3, LGALS3, SLPI, OAS3, CASP4, ZC3H12A, LCN2, TLR2	0.01872541770445608
Enrichment Score: 3.0652006117499124			
Term	PValue	Genes	FDR
GO:0005578~proteinaceous extracellular matrix	7.86993046157755E-8	CCBE1, VWF, MMP3, LTBP2, LAMC2, TNFRSF11B, MMP8, NTN1, MMP10, WISP2, MMP12, BCAN, LGALS3, MMP13, PTPRZ1, TIMP3, HPSE	5.1154548000254075E-6
GO:0031012~extracellular matrix	1.0904983267609749E-6	TINAGL1, VWF, SERPINE1, MMP3, LTBP2, MMP8, CLU, MMP10, MMP12, LGALS3, PLSCR1, MMP13, SLPI, TIMP3, LMCD1	5.100221264313128E-5
Enrichment Score: 2.605301978949154			
Term	PValue	Genes	FDR
GO:0006955~immune response	1.9461300459952305E-8	CD74, TINAGL1, TNFRSF9, H2-K1, LIF, CXCL1, TNFRSF11B, CXCL5, CXCL10, IL6, PLSCR1, CCL7, SLPI, OAS3, CCL2, SH2D6, TLR2	1.2893111554718401E-5

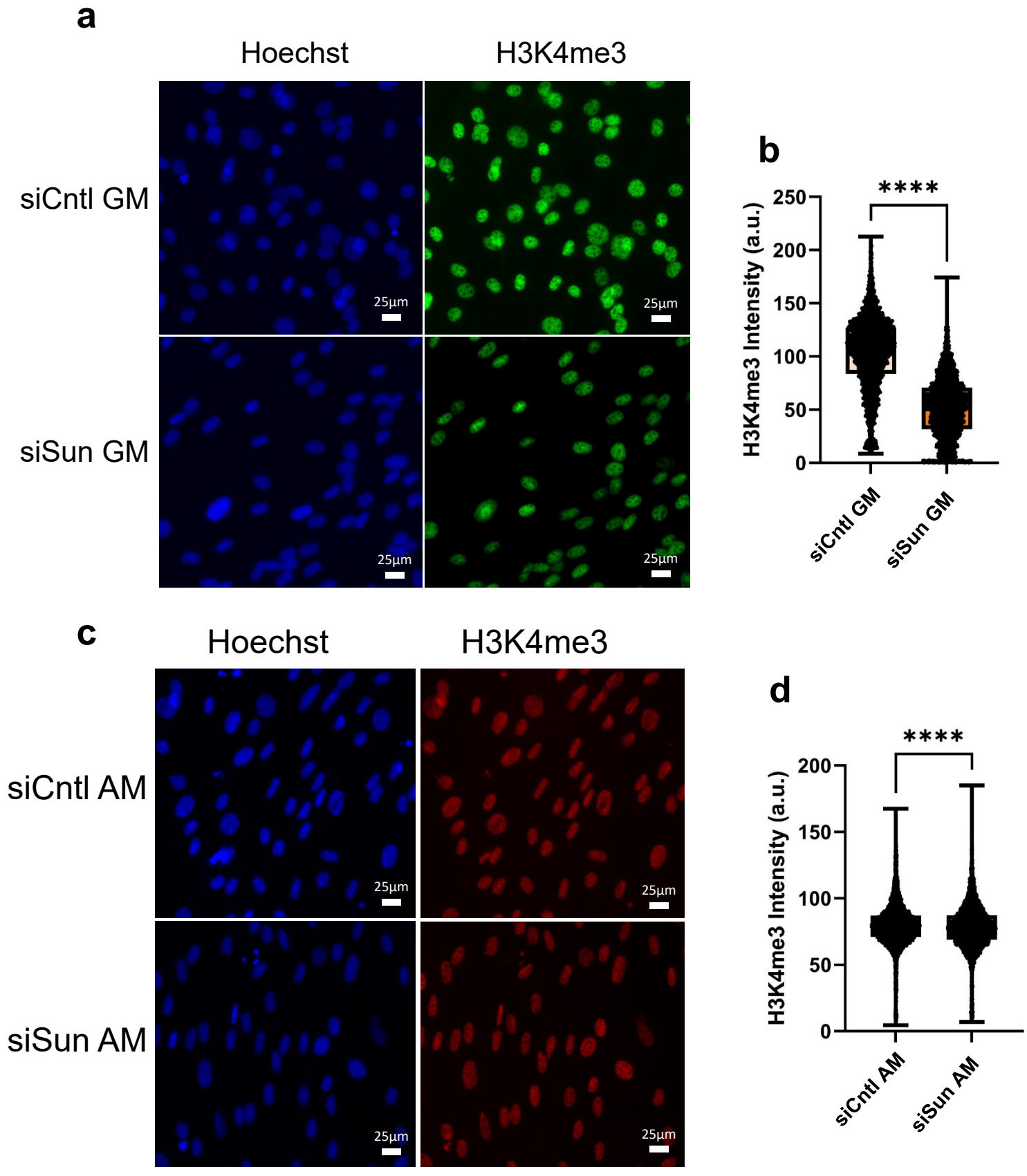

Fig. S9: Image Analysis of H3K4me3 in MSCs during treatment of siSun or siCntl. a Representative fluorescent images of Nuclei (Hoechst) and H3K4me3 (green) in siSun and siCntl treated MSCs grown in GM. **b** Analysis of florescence intensity for H3K4me3 shows 56% reduction of H3K4me3 intensity in siSun GM compared to siCntl GM (n = 2400, P < 0.0001). **c** Representative images of nuclei (Hoechst) and H3K4me3 (red) of siSun AM vs siCntl AM. **d** Analysis of H3K4me3 intensity. H3K4me3 intensity decreased by 2% in siSun AM compared to siCntl AM (n = 2500, P < 0.0001). Group analysis was made using Two-Tailed Students T-Test. **** P < 0.0001.

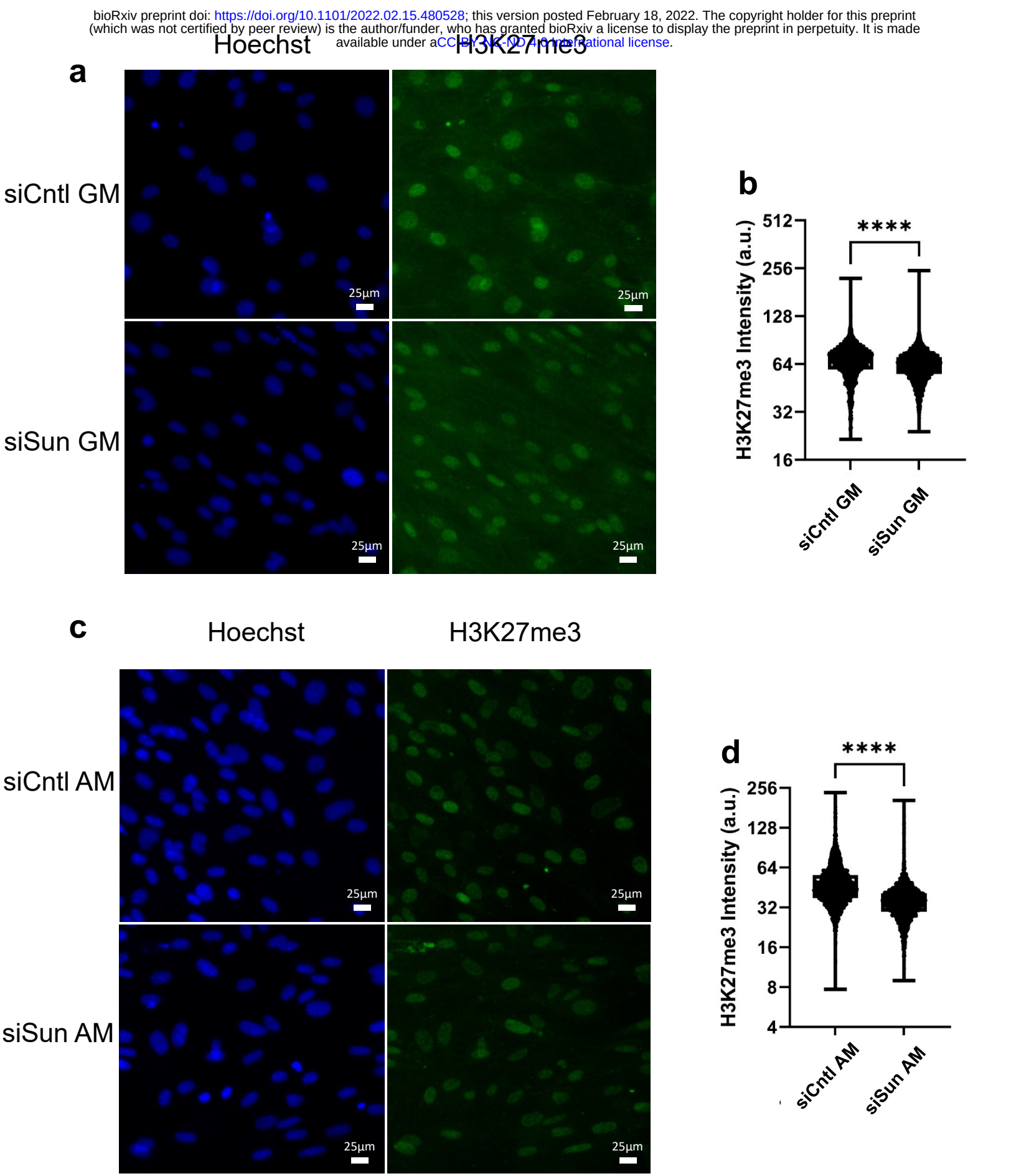

Fig. S10: Image Analysis of H3K27me3 in MSCs during treatment with siSun or siCntl. a Representative fluorescent images of Nuclei (Hoechst) and H3K27me3 (green) in siSun and siCntl treated MSCs grown in GM. **b** Analysis of florescence intensity for H3K27me3 shows 8% reduction of H3K27me3 intensity in siSun GM compared to siCntl GM (n = 2730, P < 0.0001). **c** Representative images of nuclei (Hoechst) and H3K27me3 (green) of siSun AM vs siCntl AM. **d** Analysis of H3K27me3 intensity. H3K27me3 intensity decreased by 41% in siSun AM compared to siCntl AM (n = 2550, P < 0.0001). Group analysis was made using Two-Tailed Students T-Test. **** P < 0.0001.

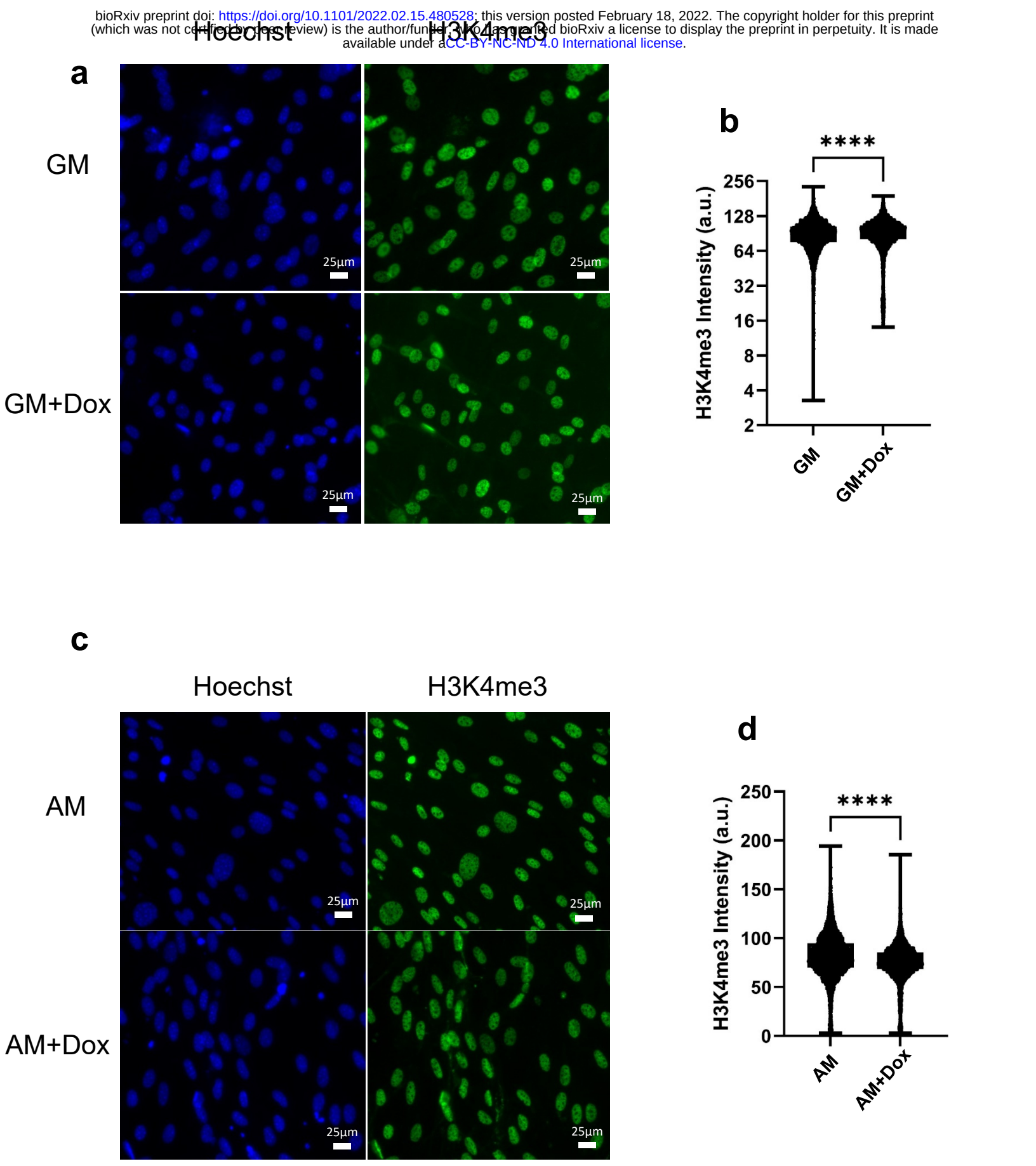

Fig. S11: Image Analysis of H3K4me3 during expression of dnKASH in MSCs. **a** Representative fluorescent images of Nuclei (Hoechst) and H3K4me3 (green) in MSCs frown in GM or GM+Dox. **b** Analysis of florescence intensity for H3K4me3 shows 4% increase of H3K4me3 intensity in GM+Dox compared to GM (n = 2900, P < 0.0001). **c** Representative images of nuclei (Hoechst) and H3K4me3 (green) of AM+Dox vs AM. **d** H3K4me3 intensity decreased by 6% in AM+Dox compared to AM (n = 2840, P < 0.0001). Group analysis was made using Two-Tailed Students T-Test. **** P < 0.0001.

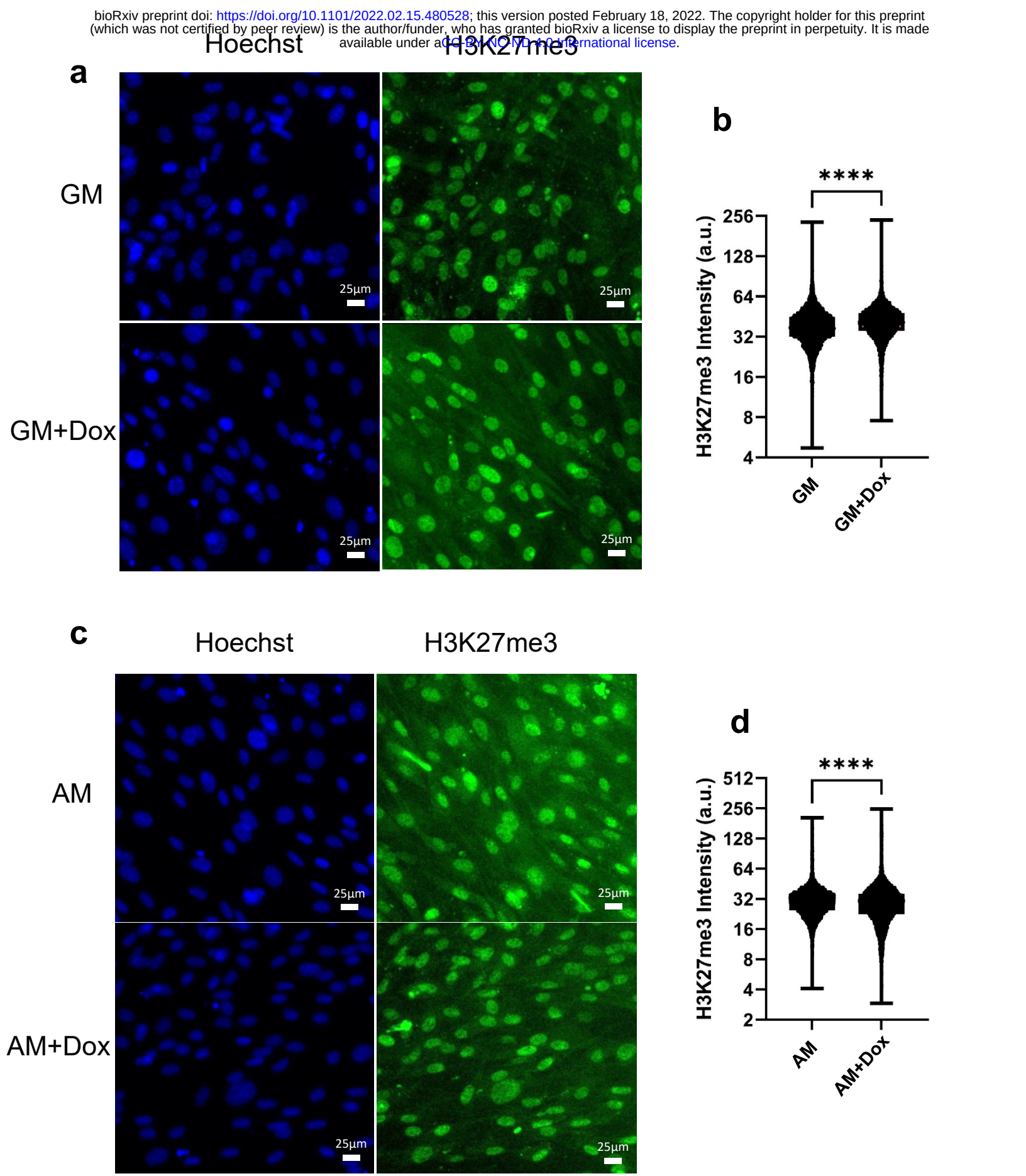

Fig. S12: Image Analysis of H3K27me3 in MSCs during expression of dnKASH. a Representative fluorescent images of Nuclei (Hoechst) and H3K27me3 (green) of MSCs grown in GM or GM+Dox. **b** Florescence intensity for H3K27me3 showed 12% increase of H3K27me3 intensity in GM+Dox compared to GM (n = 2600, P < 0.0001). **c** Representative images of nuclei (Hoechst) and H3K27me3 (green) of AM+Dox vs AM. **d** H3K27me3 intensity decreased by 2% in siSun AM compared to siCntl AM (n = 2860, P < 0.0001). Group analysis was made using Two-Tailed Students T-Test. **** P < 0.0001.

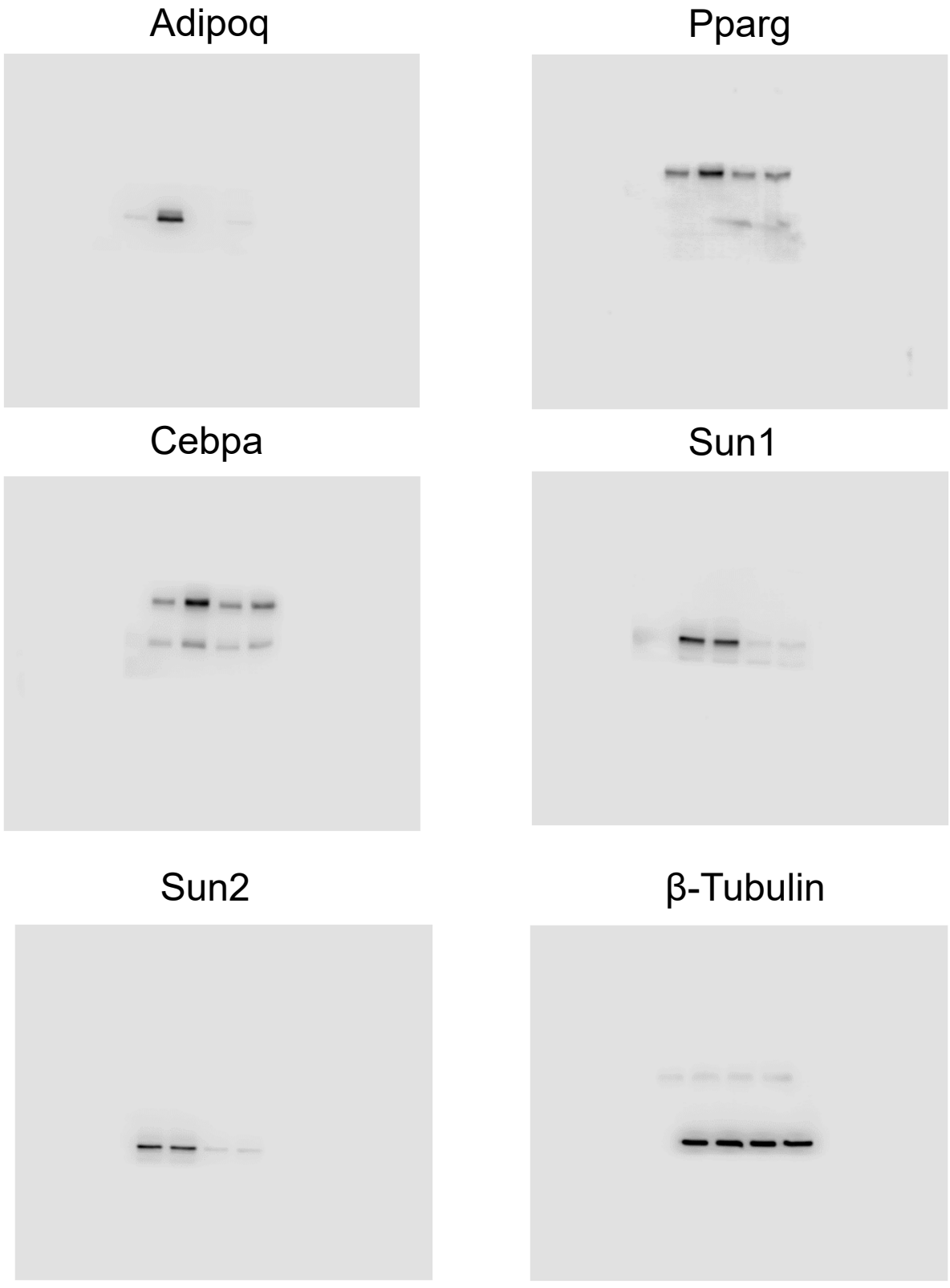

Fig. S12: Unprocessed blots for figure 3.

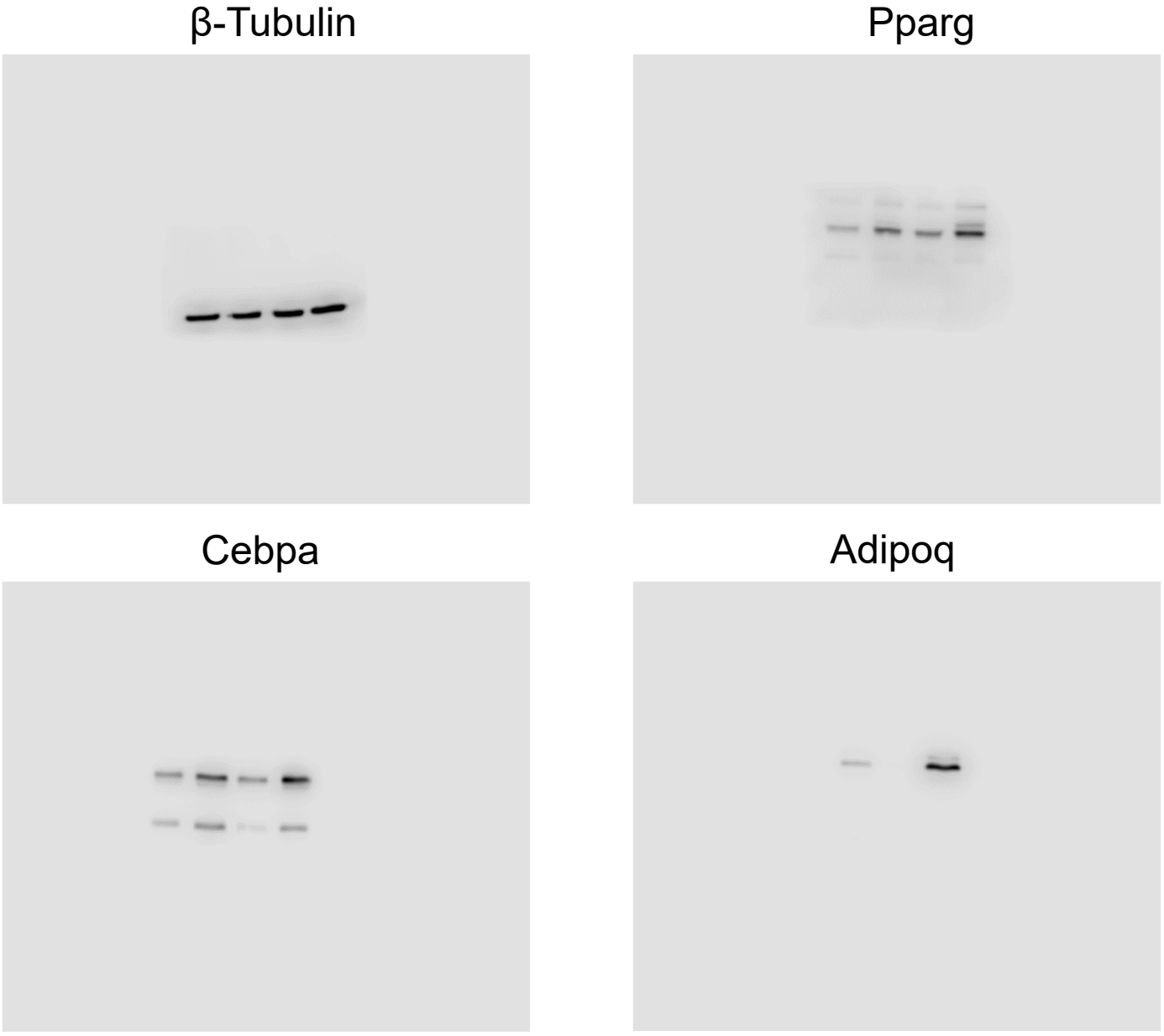

Fig. S13: Unprocessed blots for figure 4.

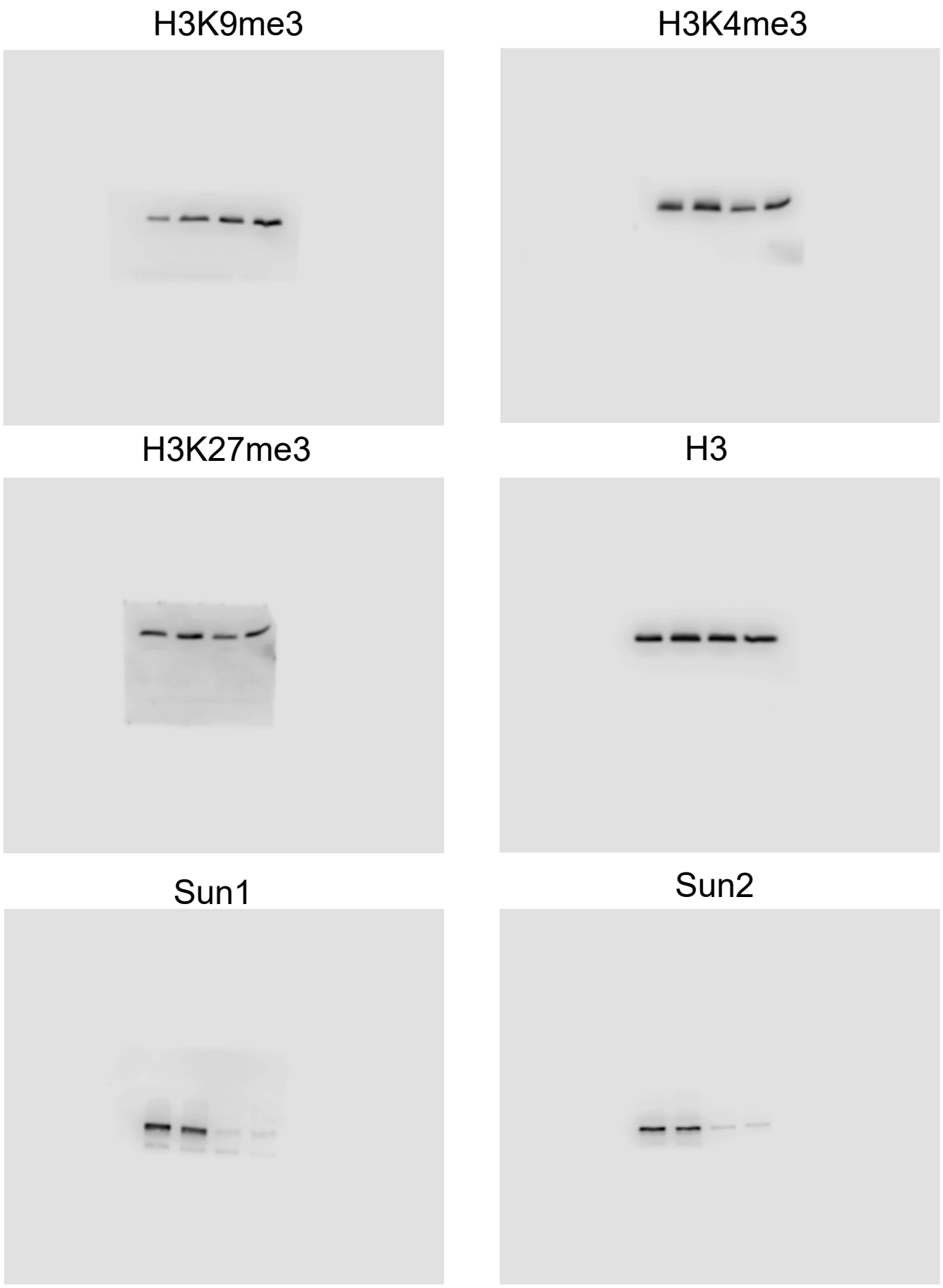

Fig. S14: Unprocessed blots for figure 5.

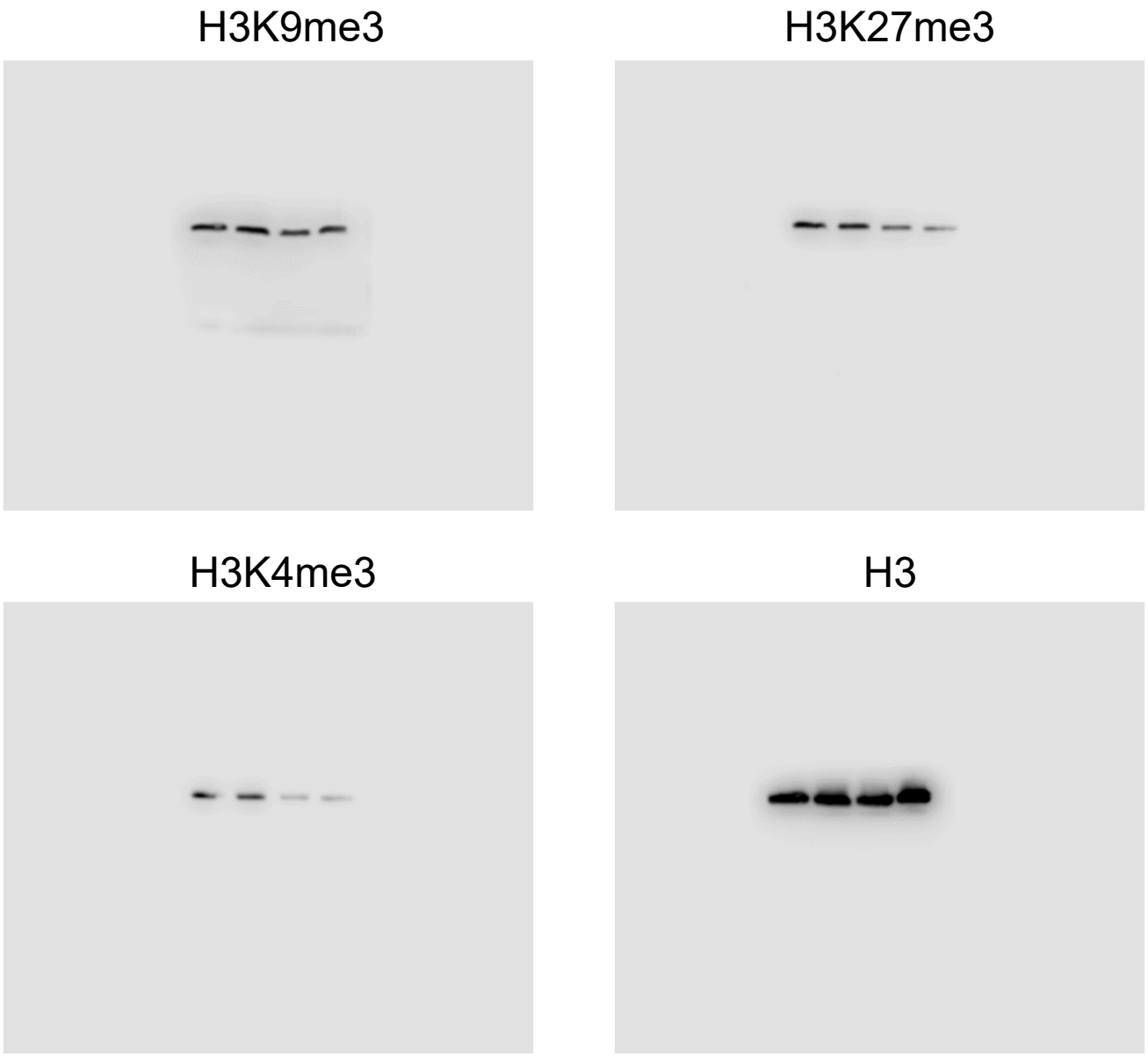

Fig. S15: Unprocessed blots for figure 6.